UNIVERSITY OF CALIFORNIA,
IRVINE

Resolving Feed-through Parasitic Capacitance in MEMS Vibratory Inertial Sensors Using EAM Technique

THESIS

submitted in partial satisfaction of the requirements
for the degree of

MASTER OF SCIENCE

in Mechanical and Aerospace Engineering

by

Crystal Wai

Thesis Committee:
Professor Andrei M. Shkel, Chair
Professor Michael McCarthy
Associate Professor Camilo Velez Cuervo

2024

DEDICATION

To my beloved parents and John Mark.

TABLE OF CONTENTS

LIST OF FIGURES

LIST OF TABLES

ACKNOWLEDGMENTS

I would like to thank my advisor Professor Andrei Shkel for providing this precious research opportunity on MEMS accelerometers and gyroscopes. I am also grateful to my thesis committee, Professor Michael McCarthy and Professor Camilo Velez Cuervo for their valuable comments and support on this work.

I appreciate this unique research experience I gained at the UCI MicroSystems Lab, and acknowledge the support from Austin Parrish, Eudald Sangenis, Lois Meira, Byungsu Chang, and Dr. Danmeng Wang. Special thanks to my close friend Davide Pavesi for valuable insights into my work.

ABSTRACT OF THE THESIS

Resolving Feed-through Parasitic Capacitance in MEMS Vibratory Inertial Sensors Using EAM Technique

By

Crystal Wai

Master of Science in Mechanical and Aerospace Engineering

University of California, Irvine, 2024

Professor Andrei M. Shkel, Chair

This MS thesis studies how to resolve the feed-through parasitic capacitance always present in MEMS vibratory capacitive sensors. MEMS capacitive sensors have been integrated into various applications due to their compact size, low power consumption, and compatibility with IC components. However, feed-through parasitic capacitance is a major issue that directly impacts the actual sensor reading, especially for miniaturized sensors. The unintended capacitance readings can result in measurement inaccuracies and degrade the signal-to-noise ratio (SNR). Electromechanical Amplitude Modulation (EAM) technique is used in this thesis to address the issue caused by feed-through parasitic capacitance within the sensors.

EAM technique involves modulating a carrier signal and an AC driving signal to the sensor. A high-frequency carrier signal is applied to the sensor, modulating the sensor outputs to a higher-frequency region as sidebands of the carrier signal. This approach isolates the motional signal of the sensor from parasitic capacitance and background noise. The motional sensor output can be then reconstructed through demodulation and filtering. The modeling results were confirmed experimentally to mitigate the parasitic capacitance from the true sensor output using the EAM technique.

Two MEMS vibratory capacitance sensors were the focus of this thesis for experimental vali-

dation of the EAM technique: an Epi-Seal Toroidal Ring Gyroscope (TRG) and a Frequency-Modulated (FM) Accelerometer. The experimental setup consists of trans-impedance amplifiers, a control feedback loop with a Phase-Locked Loop (PLL), and Automatic Gain Control (AGC) to maintain the sensor in self-resonance with consistent amplitude and phase. Key performance metrics of the MEMS sensors were extracted, including the resonance frequency, quality factor, sensitivity, and noise parameters from Allan deviation analysis. The results of both sensors confirmed that the EAM technique can mitigate and increase the SNR of the sensor, improving the performance and sensitivity of the MEMS vibratory capacitive sensors.

Chapter 1

Introduction

1.1 Motivation

MEMS inertial sensors, including accelerometers and gyroscopes have been widely used in multiple applications, ranging from navigation systems to consumer products and the automotive industry. These sensors offer advantages, such as low price, compact size, and the potential for mass production. The development of MEMS sensors focuses on enhancing sensitivity and developing cost-effective fabrication techniques. Compared with other sensor technologies, MEMS capacitive sensors consume less power, have low-temperature sensitivity, low noise, and minimal drift [8, 9]. More importantly, they are compatible and can be seamlessly integrated with CMOS (complementary metal-oxide semiconductor) electronics components for miniaturized devices and improve sensor performance with signal processing circuitry [10].

Parasitic capacitance exists between any conductive contacts that have an electrical potential difference, and it is more pronounced in MEMS devices due to their compact size. The presence of parasitic capacitance in the MEMS sensor leads to inaccurate measurements

in sensor output. This presents a major concern for MEMS capacitance sensors, which rely on changes in capacitance to detect acceleration. The detected sensor signal becomes indistinguishable between the parasitic capacitance and the actual detected sensor output. Various factors can contribute to the total parasitic capacitance from the packaging to the device structure. This unwanted parasitic effect can introduce noise, amplitude variations, and temperature bias drift in the sensor [11].

Extensive studies have been conducted on different strategies to mitigate and reduce the parasitic capacitance in MEMS capacitive sensors using signal processing, device geometry optimization, and circuit design [12, 13, 14]. Electromechanical amplitude modulation (EAM) is used in the thesis by applying a high-frequency carrier signal to the sensor and modulating the motional signal of the sensor [15]. Necessary filtering and front-end electronics are incorporated with the EAM technique to improve the signal-to-noise ratio (SNR) and eliminate parasitic capacitance from the sensor output. More information on the EAM technique can be found in Chapter 2 and [15].

1.2 Literature Review

This section presents different types of existing MEMS accelerometers. MEMS accelerometers can be categorized into 5 categories: piezoelectric, piezoresistive, capacitive, tunneling, and optical.

Piezoelectric

MEMS piezoelectric accelerometers operate on the principle of the piezoelectric effect, which converts mechanical stress into an electrical signal through the piezoelectric material. The typical structure of a MEMS piezoelectric accelerometer contains a proof mass, flexure,

and piezoelectric material [16, 1, 17]. The core materials for piezoelectric effects are Lead Zirconate Titanate (PZT) or Aluminum Nitride (AIN), which convert mechanical stress to electrical response. These materials are usually deposited on the substrate and configured in structures similar to cantilever beams or L-shaped beams to optimize sensitivity and sensor response. When a force is exerted on the suspended proof mass made of the piezoelectric material, the mass tends to resist the acceleration and generates a proportional electrical voltage output, as illustrated in Fig. 1.1. Piezoelectric accelerometers are designed to operate without the need for a continuously supplied external power source.

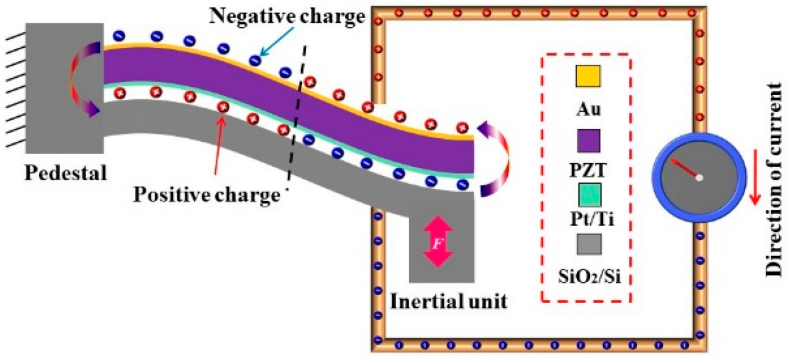

Figure 1.1: The electrical charges generated on the single cantilever beam with piezoelectric material [1]

Piezoresistive

Similar to piezoelectric accelerometers, piezoresistive accelerometers also convert mechanical stress into an electrical signal but operate on the piezoresistance effect. A piezoelectric accelerometer requires a constant voltage input for the Wheatstone bridge to compare the changes in resistance caused by acceleration [18]. A thin-film material, silicon, is used as a strain gauge, which is usually used as the arm of the Wheatstone bridge circuit with other incorporated known resistors. When an acceleration force is applied, the strain gauge within the accelerometer causes a slight deformation. It changes the electrical resistance of the strain gauge, which is used to measure the voltage change across the Wheatstone bridge

circuit. The voltage change is proportional to the acceleration experienced by the applied force.

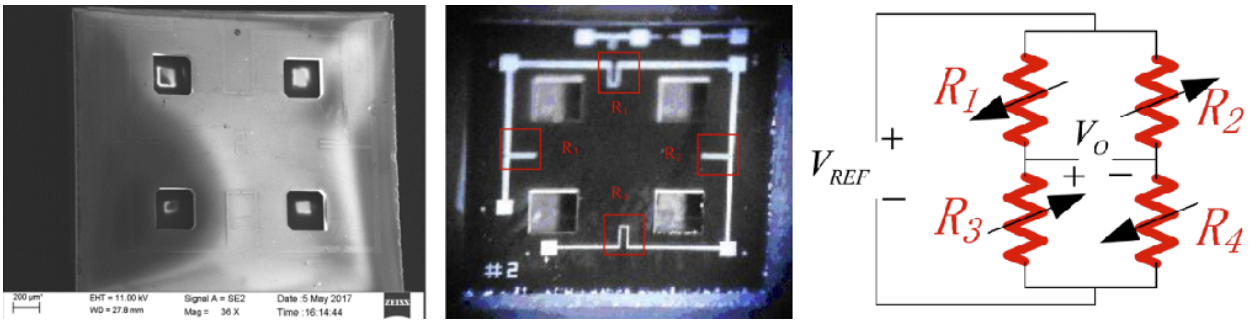

Figure 1.2: SEM photo of the piezoresistive accelerometer (Left) CCD photo of the accelerometer with resistor labeled (Center) Schematic of the Wheatstone bridge (Right)[2]

The sensitivity and performance of these accelerometers can be influenced by various factors. For instance, Chitra et al. discussed how the placement and structure of piezoresistors, such as the dimensions of the seismic mass and flexures, affect their sensitivity and dynamic range [18]. Liu et al. proposed a method by implementing high-epoxy resin in the packaging of the accelerometer for better protection in high-impact environments than traditional air packages [19]. Shi et al. demonstrated a piezoresistive structure with four flexures and a center mass that withstands and measures over 100,000 g of high shock [2], as shown in Fig. 1.2. The design and packaging of piezoresistant accelerometers have been tailored to enhance their sensitivity and ensure robustness under various operating conditions. The applications of these accelerometers range from diagnostic systems to high-shock environments, demonstrating their high range sensitivity and versatility in different fields.

Capacitive

The capacitive accelerometer measures the changes in capacitance between the proof mass and fixed micromachined plates, similar to a mass-spring system. A typical capacitive accelerometer consists of springs, proof mass, and detective plates, as depicted in Fig. 1.3. Sensing micromachined plates can be used for capacitive detection and can be divided be-

tween micromachined parallel plates and comb drives [20]. When the accelerometer is at rest, a known capacitance is detected between the proof mass and the detection plates. Once acceleration is applied, the gap between the proof mass and detection plate changes, causing a change in the capacitance. The changes in capacitance are then processed in a circuit from the capacitance change to a voltage output proportional to the acceleration. Compared with other types of MEMS accelerometers, capacitive accelerometers have lower cost, power consumption, compactness, and ease of integration with consumer electronics such as wearables and smartphones.

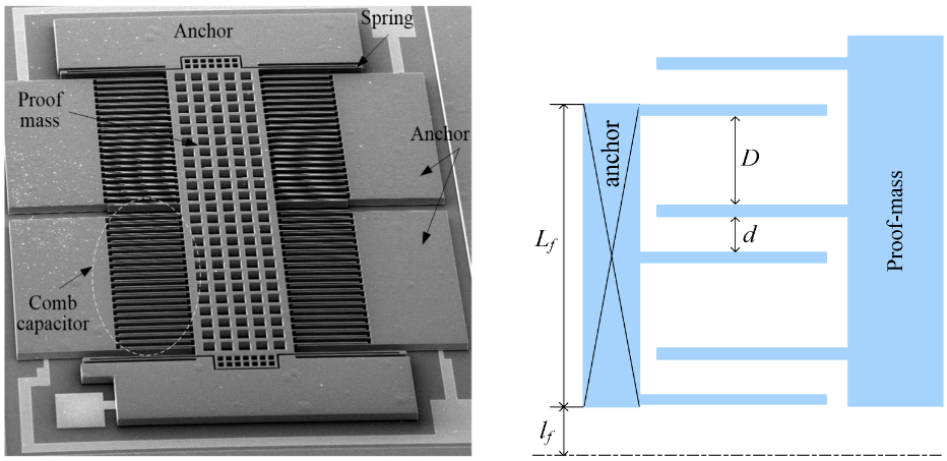

Figure 1.3: An example of a capacitive accelerometer with a comb drive structure as the detecting mechanism [3]

Tunneling

Tunneling accelerometers are a cutting-edge type of MEMS accelerometer that is still under development. The operating principle for this type of accelerometer is based on the quantum mechanics of electron tunneling. The structure of the tunneling accelerometer is similar to that of a cantilever beam, as shown in Fig. 1.4. Electrons attempt to tunnel through the gap between the tip and bottom electrodes. A feedback loop is implemented to maintain a constant current for the tunneling current and to adjust the required forces proportional to the acceleration. The current flow between the electrodes remains constant when no

acceleration is applied. Acceleration causes a measurable change in the current flowing through the tunneling electrodes.

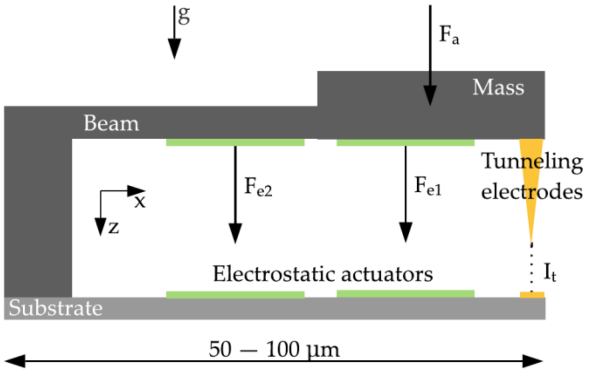

Figure 1.4: Principles of the tunneling accelerometer including a traditional cantilever beam design with adjustable electrostatic actuators and tunneling electrodes for detection [4]

Haub et al. demonstrated the use of a tunneling accelerometer with a combination of tunneling electrodes on the tip and electrostatic actuators to maintain the deflection of a beam-like structure [4]. The electrodes were maintained at a constant distance between the tunneling electrodes while detecting changes in the current. The current is highly sensitive to small deflections in the subnanometer range.

The advantages of this type of accelerometer include its high sensitivity and low-noise measurement for low-g applications. However, as a relatively novel technology, the tunneling accelerometer is still in the early stages compared to more established types, such as capacitive and piezoelectric accelerometers, which have already entered commercial use. Tunneling accelerometers demonstrated the potential of achieving high-sensitivity measurements.

Optical

MEMS optical accelerometers combine the technology of silicon micromachining with optical sensing to overcome the limitations of both technologies. This integration results in optical devices with outstanding linearity and great immunity to electromagnetic interference (EMI)

and noise [8]. The working principle of an optical accelerometer is based on optical interference or other optical phenomena to measure acceleration. There are several types of optical MEMS accelerometers, including interferometric, waveguide, grating interference, and fiber optics [20]. Xin et al. proposed an ultracompact single-layer optical MEMS accelerometer [5]. The design includes a proof mass, springs, and silicon nanowaveguides on an SOI wafer, as depicted in Fig. 1.5. This device can detect acceleration through evanescent coupling and optical confinement within waveguides. Lu et al. developed an optical MEMS accelerometer to detect changes in the interference pattern of a grating, which is measured by a photodiode [21]. The sensor demonstrated high sensitivity at 2485 V/g with a noise floor of 186 $ng/\sqrt{Hz}$. Fourguette et al. presented a type of fiber optic device that uses fiber optics to detect the changes in light caused by mass movement. The device was capable of detecting acceleration as low as 10 ng [22]. Both optical and tunneling MEMS accelerometers can achieve high sensitivity for applications requiring precise acceleration measurements. These types of accelerometers are mostly used in specialized applications and are considered a developing technology that will require further study to expand their commercial use in the future.

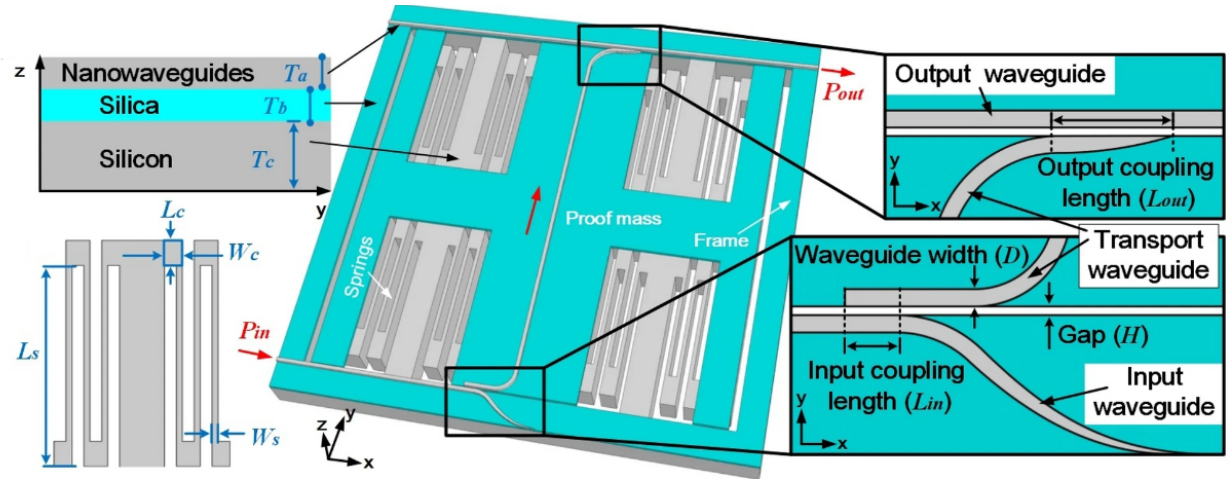

Figure 1.5: An example of an optical MEMS accelerometer combining SOI fabrication technique and optics sensing mechanism [5]

1.3 Thesis Outline

The thesis is divided into five chapters and two supporting appendices. Chapter 1 provides the motivation and background on parasitic capacitance in MEMS capacitive sensors, along with a literature review of MEMS accelerometer sensor types. Chapter 2 focuses on mitigating feed-through parasitic capacitance using the Electromechanical Amplitude Modulation (EAM) technique and includes a Simulink simulation for the signal processing path to obtain accurate sensor output. Chapter 3 details the experimental setup and performance evaluation of an Epi-Seal Toroidal Ring Gyroscope (TRG) using the EAM technique, discussing the implementation of Phase-Locked Loop (PLL) and Automatic Gain Control (AGC) for output signal stabilization. Chapter 4 presents the performance of a frequency-modulated (FM) accelerometer using EAM to accurately extract the resonance frequency, quality factor, sensitivity, and noise parameters of the sensor. Chapter 5 concludes the thesis with chapter summaries and suggests possible improvements for the current work.

Appendix A includes the design and development process of a fully customized, NIST-funded NEVERLOST handheld platform for firefighter indoor navigation. Appendix B provides the procedures for gyroscope operation on the Toroidal Ring Gyroscope using the HF2LI Zurich Instrument Lock-In Amplifier.

Chapter 2

Electromechanical Amplitude Modulation

2.1 Background

MEMS capacitive sensors are known for their compact size, low power consumption, and ease of integration with IC components [8]. The miniaturization of MEMS capacitive sensors brings advantages but also introduces parasitic capacitance, which affects sensor performance. Fig. 2.1 depicts undesired electrical couplings that occurred from the conductive elements within the sensor structure, including:

- Electrode-to-Electrode: Close spacing between actuation and detection electrodes
- Electrode-to-Substrate: Between the electrodes and the underlying substrate
- Interconnect: Wire connections between the sensor and the package
- Sensor-to-PCB: Signal routing between the package and the PCB through the metal pins

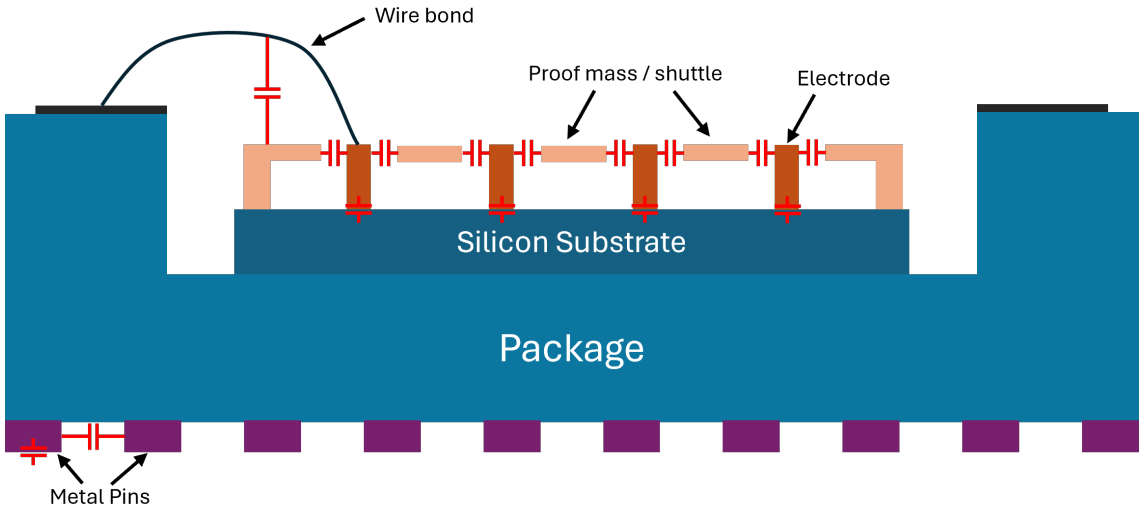

Figure 2.1: Parasitic capacitance within the MEMS sensors from the substrate, electrodes, interconnects, and the contact points between the PCB and the package

Due to the closely spaced and thin conductive elements in MEMS devices, these factors collectively add up and influence sensor performance by introducing additional noise, resulting in a low signal-to-noise ratio in the detected measurements. The unintended parasitic capacitance could be orders of magnitude higher than the motional current.

Parasitic capacitance is unavoidable, but it can be minimized by properly grounding the substrate and shielding it with insulating layers between conductive layers [15]. If the detected output signal or the pickoff signal from the electrodes is directly measured from the sensor, parasitic capacitance may degrade the signal and make it difficult to obtain the actual signal output signal, especially for high-frequency applications [23].

There are multiple ways to mitigate or remove the effect of parasitic capacitance on the signal output. One way to eliminate parasitic capacitance in the sensor signal is to use electromechanical amplitude modulation (EAM) by applying a high-frequency carrier signal [15]. The higher carrier frequency helps eliminate the parasitic feed-through from the driving AC signal. Another advantage of using EAM is its ability to easily distinguish the signal output of the sensor from noise. EAM is convenient and beneficial when assessing sensor

performance to effectively separate the actual sensor signal from unwanted noise. In the subsequent chapters, the EAM technique is used to characterize the performance of two MEMS capacitive sensors.

2.2 Working Principle

EAM is similar to amplitude modulation used in electronic communication, which involves the use of bias DC, AC signal, and carrier signal. The AC signal can also be interpreted as the modulating signal or message signal. The carrier signal has a much higher frequency than the AC signal. The AC signal and the carrier signal can be mathematically represented as follows:

$$m(t) = A_m \cos(\omega_m t) \qquad C(t) = A_c \cos(\omega_c t) \tag{2.1}$$

where A_m is the amplitude of the AC signal, ω_m is the frequency of the AC signal, A_c is the amplitude of the AC signal, ω_m is the frequency of the carrier signal. The modulation process of combining the carrier signal with the AC signal in the time domain can be represented as:

$$\begin{aligned} X_{am}(t) &= m(t) \cdot (C(t) + DC) \\ &= [A_m \cos(\omega_m t)] \cdot [A_c \cos(\omega_c t) + DC] \\ &= A_m A_c \cos(\omega_m t) \cos(\omega_c t) + DC \cdot A_m \cos(\omega_m t) \\ &= \frac{A_m A_c}{2} [\cos((\omega_c + \omega_m)t) + \cos((\omega_c - \omega_m)t)] + DC \cdot A_m \cos(\omega_m t) \end{aligned} \tag{2.2}$$

The time domain response includes the upper and lower sidebands representing the modulated motional signal, with the DC offset showing as the third term. For better visual understanding, the modulated signals are converted to the frequency domain to better un-

derstand and analyze the behavior of the carrier signals and information-carrying sidebands (AC signal) in the frequency spectrum. The time responses of the modulated signal are presented in Fig. 2.2. The modulated signal in the frequency domain taking the Fourier Transform is as follows:

$$\begin{aligned}\mathcal{F}\{X_{am}(t)\} = &\frac{A_m A_c}{4}\left[\delta(f-(f_c+f_m))+\delta(f+(f_c+f_m))\right] \\ &+\frac{A_m A_c}{4}\left[\delta(f-(f_c-f_m))+\delta(f+(f_c-f_m))\right] \\ &+\frac{DC\cdot A_m}{2}\left[\delta(f-f_m)+\delta(f+f_m)\right]\end{aligned} \tag{2.3}$$

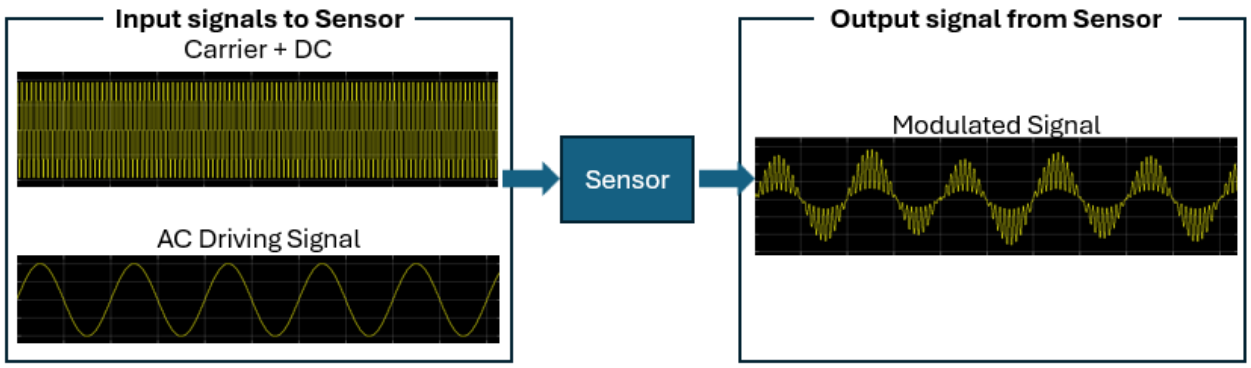

Figure 2.2: Time response of the input signals to the sensor and the modulated signal as the output from the sensor

Based on the frequency domain modulated signal, the first term represents the upper sideband, which is a summation of the carrier frequency and the AC frequency. The second term represents the lower sideband, which contains information about the carrier signal subtracted from the AC frequency. The third term is the carrier frequency with the DC offset effect. This is also observed in the Simulink output response in Fig. 2.4.

2.3 Simulink Simulation

The Simulink model represents the signal processing path using the EAM method to extract the detected motional signal of the sensor as the output. The EAM method can be organized

into three main steps: signal output from the sensor, filtered modulated signal using an analog filter, and demodulated signal using a Zurich Instrument (ZI) Lock-In amplifier. The signal amplitude and frequency used in this Simulink model are listed in Table 2.1. The Simulink model in Fig. 2.3 includes signal conditioning for the input signal. Multiple scopes are placed to view the time and frequency domains of the signal response. The blue scopes represent the time response of the signal, and the red scopes can visualize the FFT spectrum of the signal.

Signal	**Amplitude**	**Frequency**
AC Driving	1V	50kHz
Carrier	1V	1MHz
DC Offset	1.5V	n.a

Table 2.1: Input signal amplitude and frequency parameters used in the Simulink Model

2.3.1 Signal Output from the Sensor

Typical MEMS capacitive sensors include suspended features like a movable proof mass and stationary electrodes for actuation and detection anchored to a silicon substrate. The EAM technique characterizes sensors by applying three specific signals. An AC driving signal is applied to the actuation electrodes. The DC bias offset and carrier signal are combined and applied through anchor points to the structure. Detection electrodes are connected to a trans-impedance amplifier to sense changes in capacitance and convert the current to a voltage signal as the output motional signal.

In the Simulink model, an AC driving signal of 1V at 50 kHz is applied to the actuation electrodes and is picked up with the parasitic feed-through generated within the sensor. The AC driving signal is produced by the ZI Lock-In amplifier, which is also used as the reference signal in the demodulation process. Another generated signal source, a carrier signal of 1 V at 1 MHz, combined with a DC offset of 1.5 V is applied to the anchor/proof mass of

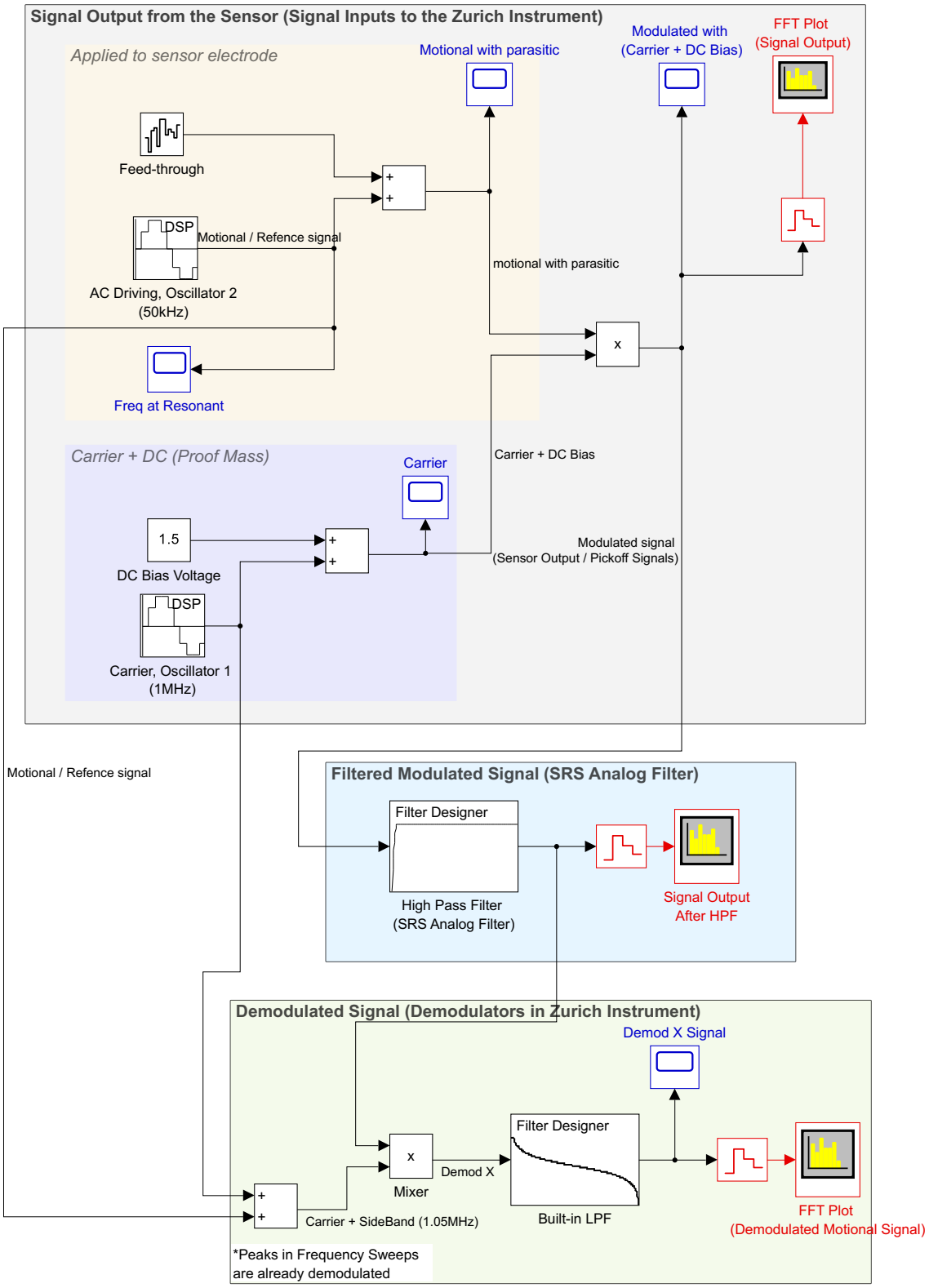

Figure 2.3: Simulink EAM Model from Signals Input into the Sensor to Demodulated Outputs from the Lock-In Amplifier

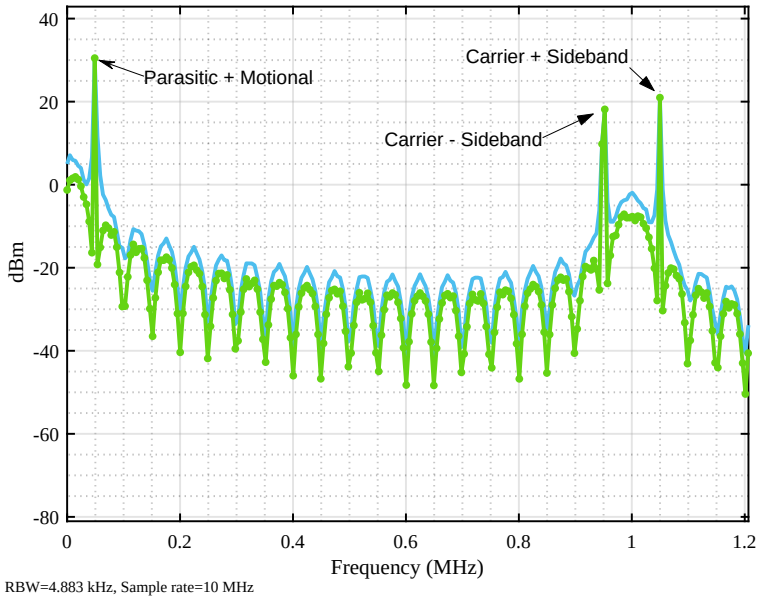

Figure 2.4: Simulink FFT Response of the sensor output

the sensor. The modulated signal is captured by the detection electrodes after mixing both signals.

The FFT plot of the signal output from the sensor is analyzed and presented in Fig. 2.4. The motional signal with parasitic feed-through can be seen at 50kHz. The modulated signal includes three peaks: the carrier signal and its information-carrying sidebands at 0.95 MHz and 1.05 MHz. These sidebands are located at the carrier frequency plus and minus the motional frequency. The DC bias offset affects the carrier signal amplitude in the modulated signal, resulting in a lower amplitude compared to the sidebands. This also explains the three terms in Eq. 2.3 with lower and upper sidebands in the first two terms and how the DC bias offset affects the amplitude of the carrier signal.

2.3.2 Filtered Modulated Signal Using Analog Filter

The modulated signal is passed through an adjustable analog filter to remove lower-frequency region frequencies and leave only the modulated components at a higher frequency, as shown

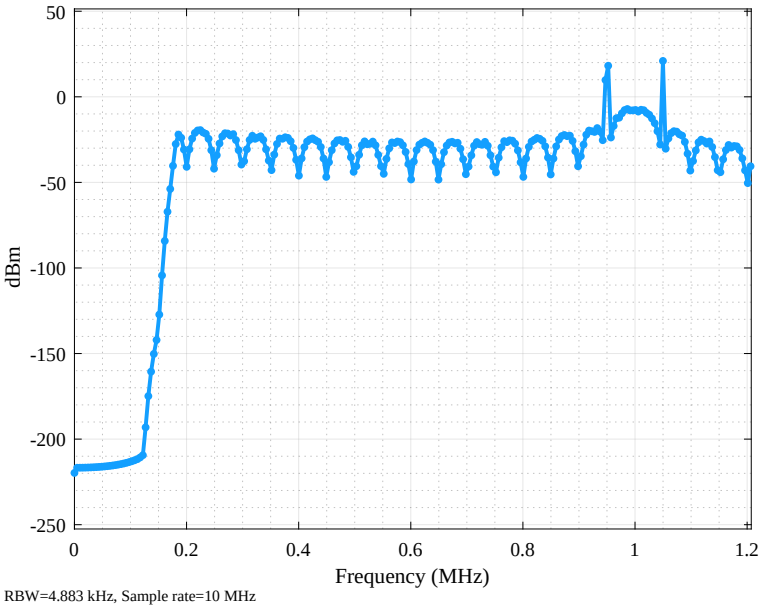

Figure 2.5: Simulink FFT response after high pass filter is applied to remove the motional signal with parasitic capacitance

in Fig. 2.5. The analog filter takes out the low-frequency noise from the environment, the motional frequency with feed-through parasitic capacitance, and the DC offset at 0 Hz. This process enhances the demodulation process at a later stage by preserving the sideband content, which contains the motional information of the signal, and removing unrelated components. The modulated signals after passing through the high-pass filter can be verified with the measured modulated signal input in the ZI Lock-in amplifier before demodulation, as illustrated in Fig. 2.6. AC coupling is enabled in the Lock-in amplifier to reject any DC input in the signal. Therefore, the carrier amplitude shown in the plot is higher than that of the sidebands.

2.3.3 Demodulated Signal Output Using the Lock-In Amplifier

After mixing the signals in the sensor and filtering out the unwanted parasitic feed-through signals, the actual motional signal can be reconstructed by demodulating the signal. The sidebands contain the information for the motional signal, the modulating signal can be

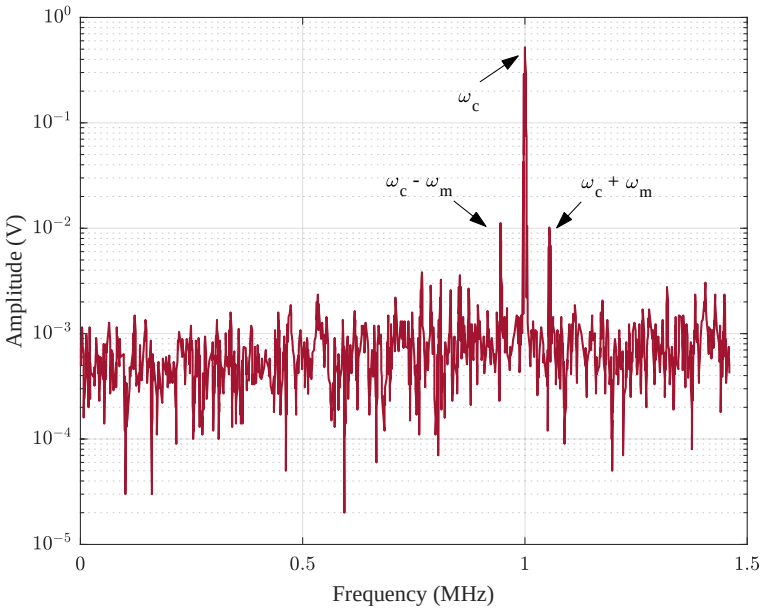

Figure 2.6: Measured modulated signal from the Lock-in Amplifier after using the high pass filter

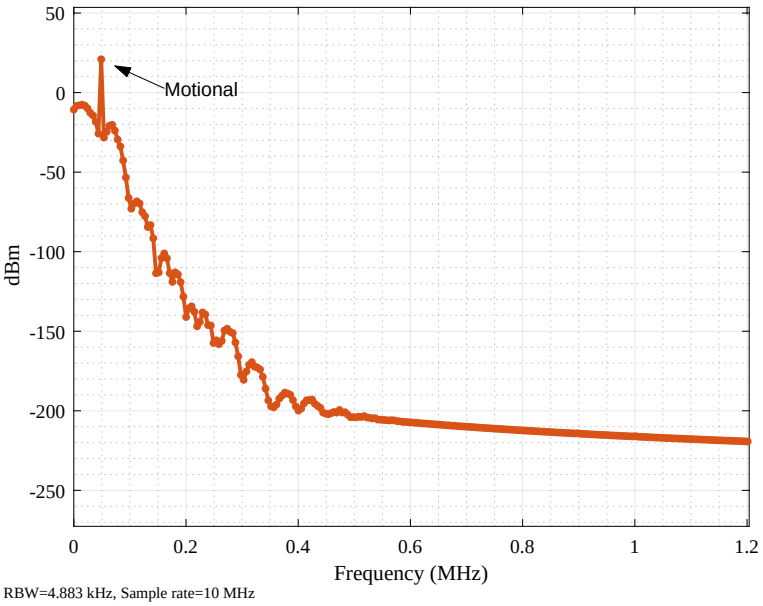

Figure 2.7: Simulink FFT Response after signal is demodulated with motional peak without the parasitic capacitance

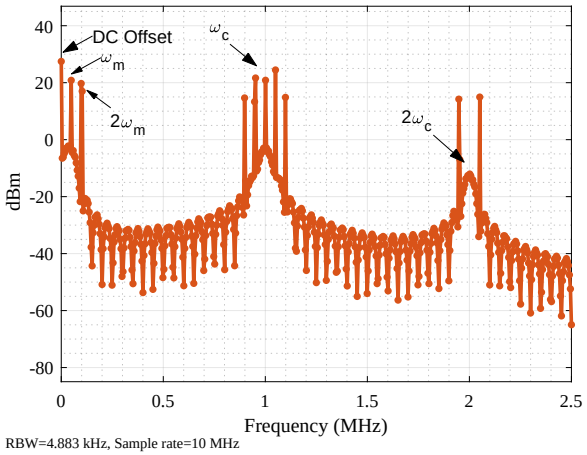

Figure 2.8: Demodulated Signal without using low pass and high pass filter

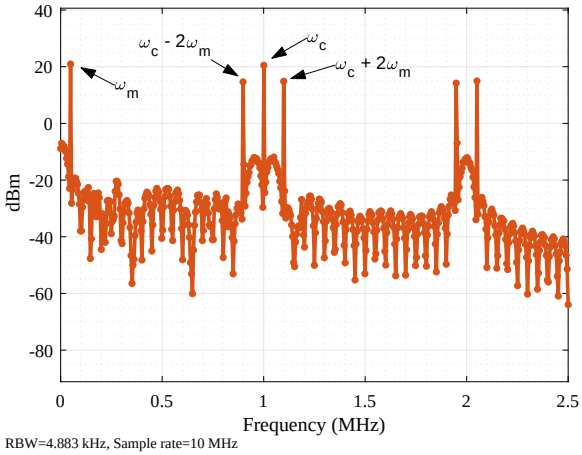

Figure 2.9: Demodulated Signal without using low pass filter

demodulated at either sideband frequency: carrier plus AC driving or carrier minus AC driving frequency. Both the AC driving signal and the carrier signal are generated as signal inputs to the sensor. The same signals are used as reference signals to demodulate the filtered modulated signal by mixing them to rebuild the motional signal, as shown in Fig. 2.9. However, further filtering is needed after demodulation. The demodulated signal still includes high-frequency components at the carrier frequency, along with the harmonics of the carrier frequency and its sidebands. The low-pass filter is a part of the lock-in amplifier to help remove noises that are not related to the signal of interest. The FFT plot of the demodulated signal after applying the low-pass filter is shown in Fig. 2.7. Without the high-pass filter before demodulating the modulated signal, the demodulated output can also result in more harmonics or unwanted frequency components, as depicted in Fig. 2.8. Therefore, filtering with high-pass filters and low-pass filters is important in modulation and demodulation processes to better extract the motional signal of the sensor.

2.4 Conclusion

This chapter discusses the EAM technique to reduce feed-through parasitic capacitance in MEMS capacitive sensors. A high-frequency carrier signal is mixed with an AC driving signal at the resonance frequency of the sensor. The motional sensor signal is shifted to a higher frequency region as the sidebands of the carrier signal, isolating it from feed-through parasitic capacitance and noise. A Simulink simulation demonstrated the modulation, demodulation, and filtering processes to completely remove the unwanted signals. This technique can be applied to MEMS sensors and will be further validated on a gyroscope and an accelerometer in Chapters 3 and 4.

Chapter 3

Toroidal Ring Gyroscope

In the previous chapter, an in-depth explanation and simulation of electromechanical amplitude modulation (EAM) were discussed, focusing on extracting the pickoff signals to mitigate the parasitic feedthrough of the sensors. This chapter primarily demonstrates the use of the EAM technique on a MEMS gyroscope to actuate and obtain the performance characteristics of the sensor.

3.1 Introduction

MEMS gyroscopes leverage miniature vibrating structures to sense rotations. This functionality relies on the Coriolis effect, which generates measurable force in response to rotation. These gyroscopes are also known as Coriolis Vibratory Gyroscopes (CVG). CVGs can be classified into two types: type I with a symmetrically shaped structure and type II with a mass-spring system [24]. Senkal et al. introduced a type I CVG, the first Toroidal Ring Gyroscope (TRG) with a 2-D silicon ring structure as depicted in Fig. 3.1 [6]. The symmetrical ring structure of the TRG significantly minimizes energy loss within the system.

This gyroscope features a circular outer anchor connected to a symmetric ring resonator, which functions as the spring of the system. The vibration energy is focused on the inner circle, where electrodes are positioned to actuate and detect sensor movement. A key advantage of the toroidal ring geometry is its ability to concentrate vibrational energy within the rings, thereby minimizing energy dissipation at the outer anchor points and achieving a high-quality factor.

The operating principle of the TRG can be similar to the movement observed in a vibrating wineglass. An AC exciting signal applied to the exciting electrodes causes the inner ring to vibrate in a "wineglass mode", similar to the shape of n = 2, as illustrated in Fig. 3.2 [7]. Detection electrodes capture an electrostatic force from the deflected vibrating ring and convert this force into the device's output response. When the Coriolis effect influences the vibrating ring, a slightly deformed shape of the ring is detected. Yusheng et al. have experimentally demonstrated a TRG featuring an Epitaxial Silicon Encapsulation process (Epi-seal) with a simulated resonant frequency of 68.7 kHz and an experimentally tested frequency of 54.5 kHz [25]. An important advantage of the Epi-seal device is its capability to function in ambient conditions without requiring a vacuum chamber for sensor actuation [26].

The Epi-Seal TRG was selected for demonstration in this study due to its ease of actuation in ambient conditions. These devices feature 16 electrodes for differential actuation and detection, with the electrode locations labeled according to the desired gyroscope features. The device can actuate in n = 2 and n = 3 modes, depending on which electrodes are connected to the LCC socket [6]. For simplicity, the n = 2 mode was chosen for actuation, with an expected natural frequency of around 54.7 kHz, previously characterized for this TRG device. Fig. 3.3 illustrates the differential electrode locations necessary for the TRG device to actuate in the n = 2 mode, including forcing (F) and sensing (P) electrodes in the X and Y directions. The tuning electrodes, placed between the driving and sensing electrodes,

can be used to measure bias instability and scale factors.

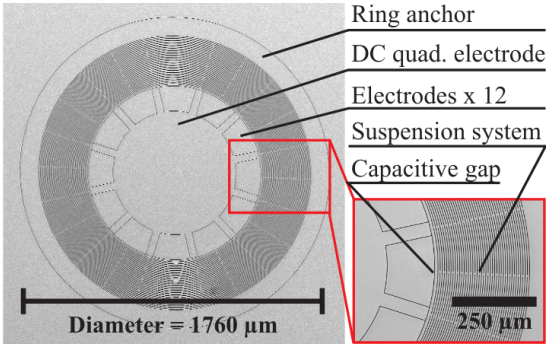

Figure 3.1: Structure of the Epi-seal TRG [6]

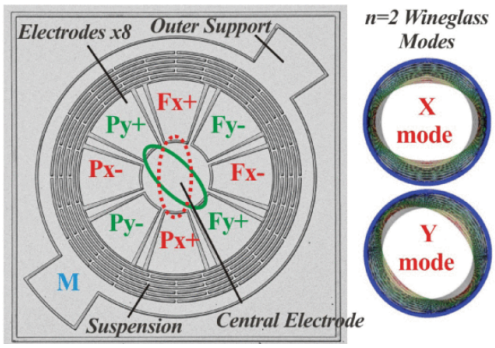

Figure 3.2: n = 2 TRG Wineglass Mode-shape [7]

3.2 Experimental Setup

This section details the experimental setup required for the TRG device used in this study. The wire bonding techniques of the device and integration with the front-end electronics to the ZI HF2LI lock-in Amplifier are described. The components of the drive-axis feedback control loop employed in the ZI lock-in amplifier is also explained.

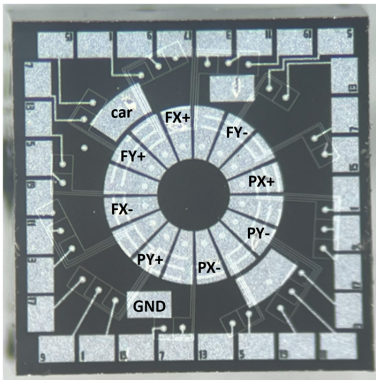

Figure 3.3: Epi-Seal TRG device with forcing and pickoff electrodes used for n=2 mode actuation and detection

3.2.1 Wire Bonding

The primary objective of wire bonding is to establish electrical connections between the device and the leadless chip carrier (LCC) package, where the device is housed for electrostatic actuation. The wire bonding diagram is dependent on the locations of the front-end PCB pins. To confirm a good electrical connection between the LCC pins and the signal inputs/outputs of the board, electrical continuity was checked using a multimeter. Multiple wire boning diagrams were drawn to determine the best orientation and minimize cross-wiring for all the soldered electrical components soldered on the PCBs. In this study, the wire bonding diagram was created using the QMG-P3 front-end PCB for the optimal orientation and shortest electrical routing for the TRG, as illustrated in Fig. 3.4 for the wire-bonded TRG. Rethreading the wire bonding machine and achieving precision in wire bonding requires a lot of practice to ensure reliable connections. Some precautionary measures during the wire bonding process include using shorter wire connections to minimize parasitic capacitance and avoiding cross-wiring to prevent potential shorts in the sensor. Several practice sessions were conducted using the bonding machine by wirebonding on a TRG dummy die first. The actual TRG device was then wire-bonded after several practice runs.

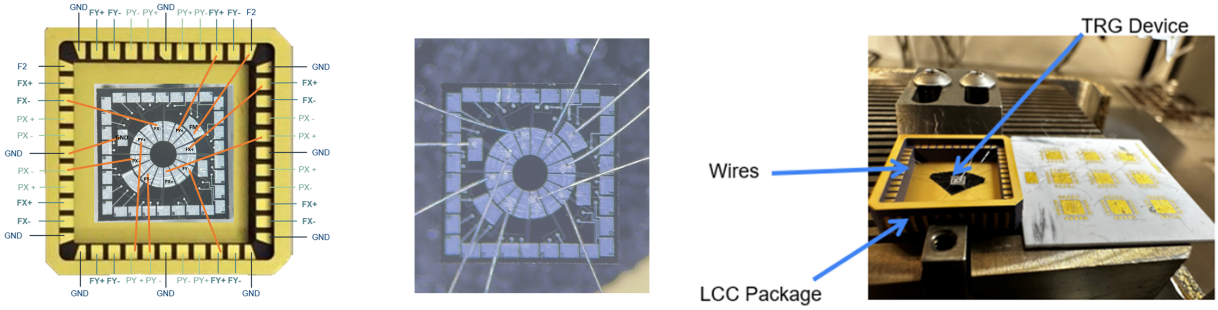

(a) (b)

Figure 3.4: (a) TRG wire bonding map using the "QMG-P3" Top Front-end Electronic (b) Picture of a wire Bonded TRG on the LCC Package

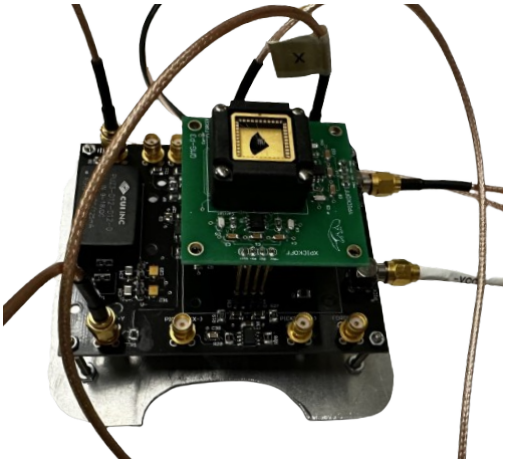

Figure 3.5: Wire Bonded TRG device secured in the LCC package with top (QMG-P3) and bottom front-end electronics

3.2.2 Instrumentation Setup

The experimental setup comprises a wire-bonded gyroscope (TRG), front-end electronics, and a lock-in amplifier from Zurich Instrument (ZI). The setup of the TRG in LCC integrated with the front-end electronics is shown in Fig. 3.5. The wire-bonded TRG is placed in the LCC package and inserted on the "QMG -P3" PCB. This top front-end electronics platform is equipped with trans-impedance amplifiers to convert the detected current reading to voltage signals. The bottom front-end electronics mainly amplify the pickoff signals from the top PCB and the forcing signals input to the TRG. BNC cables were connected following the interconnection diagram between the ZI Lock-In Amplifier and the bottom front-end electronics, as shown in Fig. 3.6. The pickoff electrodes (PX+, PX-, PY+, PY-) from the TRG were amplified through the front-end electronics and connected to the differential signal input connectors on the ZI lock-in Amplifier. The AC driving signal is generated from the output from Signal Input 1 of the Lock-In Amplifier and links to either Forcer X or Forcer Y to excite the sensor through its driving electrodes. It can only excite the TRG on one axis at a time, limited by the output channels of the ZI lock-in amplifier. The carrier signal is generated from Signal Output 2 of the ZI lock-in amplifier, and it is directly connected to the "AC" connector of the bottom front-end electronics. Analog Filters may be used between

the connections for the pickoff signals to remove unwanted noises near the frequency of the carrier signal and its sideband region.

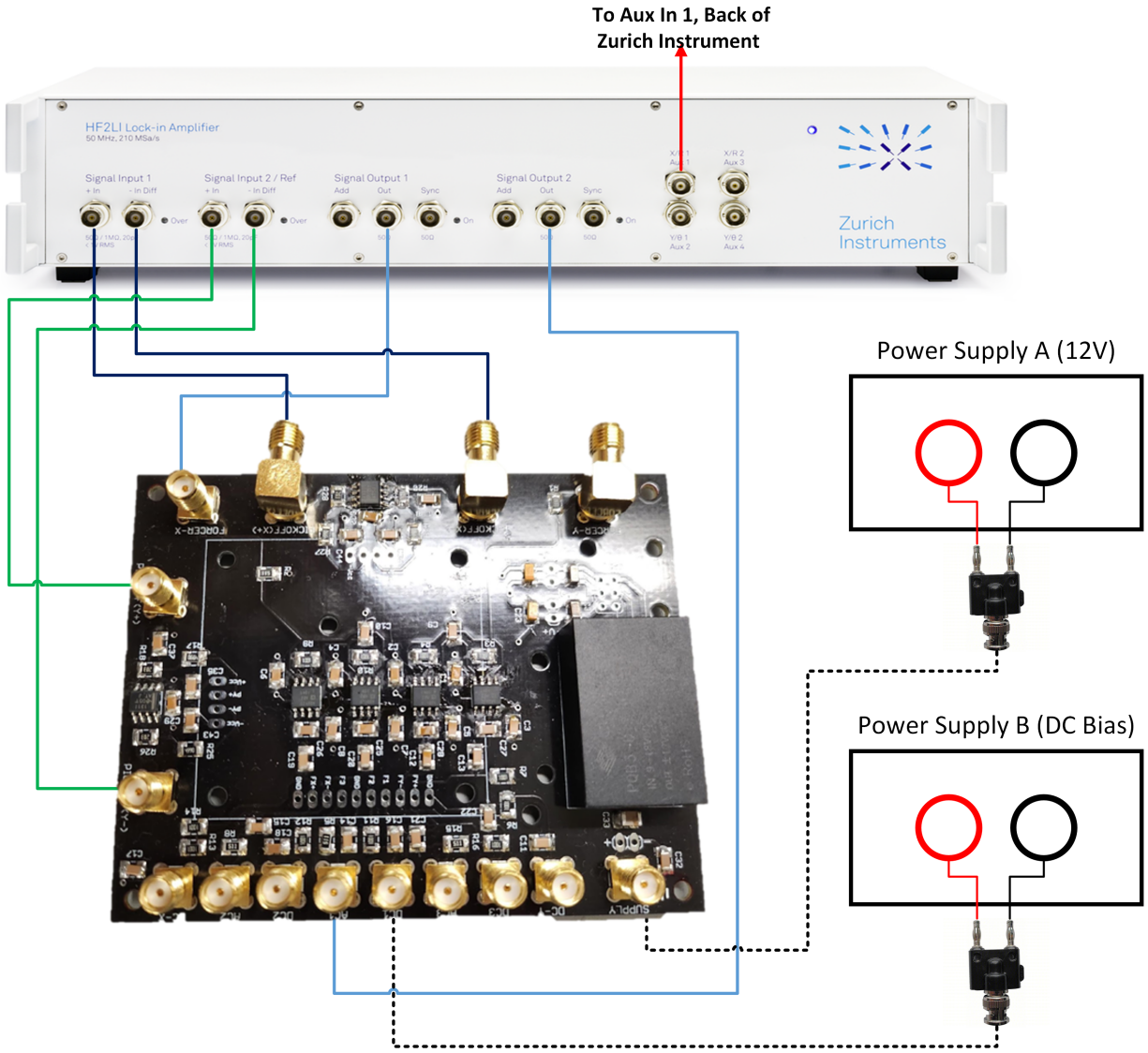

Figure 3.6: Experimental Test Setup for TRG: Electrical Interconnections between front-end electronics and Zurich Instrument. Purple lines - Pickoff connections for the X-axis; Green lines - pickoff connections for the Y-axis; Black lines - External DC Power Supply; Light blue lines - generated signal outputs from the Lock-In Amplifier; Red - PLL purposes

The carrier signal and the AC driving signal were experimentally tested and tuned, started at a low voltage and adjusted to an optimal level with a clear modulated wave observed from the ZI Lock-in Amplifier. The AC driving signal was initially set to 54 kHz, a preliminary estimate based on the previously characterized value. The carrier signal was selected to

be at 1 MHz, which is nearly 20 times the expected resonant frequency of the sensor. For additional details of the step-by-step procedures for gyroscope operation and guidance on using the ZI Lock-In amplifier, refer to Appendix B. The experimental response of the TRG was captured using a 500 mV AC driving signal at 54.5 kHz and a 1 V DC bias signal in conjunction with a 1 V carrier signal at 1MHz.

3.2.3 Drive Mode Control Loop

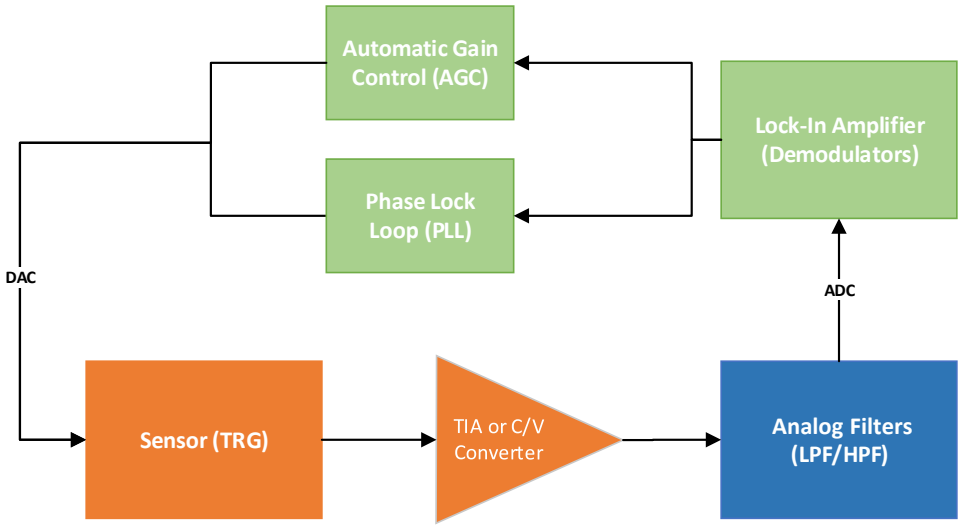

Figure 3.7: Drive mode control loop with Phase-Locked Loop (PLL) and Automatic Gain Control (AGC) to lock the phase and maintain the amplitude of the input signal to the sensor

The drive mode axis control loop for the Toroidal Ring Gyroscope (TRG) is used to maintain the sensor in self-resonance at an accurate resonance phase and constant amplitude. The elements used to achieve self-resonance actuation are depicted in Fig. 3.7. The process begins with the sensor being driven at its resonance frequency and outputs the modulated signal to the trans-impedance amplifier, which converts the current reading to a voltage output for further processing. The modulated signal is then passed through low-pass and high-pass filters to remove low-frequency noise and unwanted signals. The filtered signal is fed into a lock-in amplifier to demodulate the signal and extract the motional signal of the sensor. This

analog signal is converted into a digital signal by an ADC within the ZI Lock-in Amplifier. A phase-locked Loop (PLL) is implemented to lock onto the natural frequency of the sensor, while automatic gain control (AGC) adjusts the amplitude of the driving signal to maintain a constant sensor output amplitude. The processed control signals are then converted back into analog form by a DAC to drive the sensor and operate it at the resonance frequency and desired amplitude. The sense mode of the sensor has no control loop; it reads directly from the sense axis to provide the Coriolis rate input of the device.

Phase-Locked Loop (PLL)

A phase-locked loop (PLL) is a control feedback loop that synchronizes the frequency and phase of an input signal with a reference signal. The feedback loop maintains the stability of the demodulated signal from noise and fluctuation in the device. In the ZI Lock-in Amplifier, the PLL compares and matches the reference signal generated by the local oscillator (AC signal/Signal Output 2) with the sensor's output signal.

The detected signal consists of two demodulated components: the "in-phase" (Coriolis) component and the "quadrature" component. The Coriolis component carries the message signal of interest. The quadrature component is the error signal caused by energy leaks from the drive axis to the sense axis [27]. These components are separated by a 90-degree phase delay. The error signal is derived from the difference between the expected and actual rotation information due to the imperfection shape in the fabricated device. Using PLL after demodulation can improve the motional signal by separating the error signal from the Coriolis component.

The HF2LI ZI Lock-in Amplifier has two demodulators that can be used with PLL to adjust the frequency of the AC driving signal to the sensor [28]. The demodulator first extracts phase information from the detected signal. The PID controller then processes the error

signal from the demodulator. The numerically controlled oscillator (NCO) adjusts the output frequency based on the correction signal from the PID until the PLL is locked within an acceptable range set by the user. The goal within the PLL is to minimize the error signal, or quadrature signal, ideally bringing it close to zero.

Automatic Gain Control (AGC)

Automatic Gain Control (AGC) is used alongside the PLL to provide a constant output amplitude for the sensor. AGC achieves a fixed amplitude of the demodulated signal by constantly adjusting the input AC driving amplitude to the sensor. The trans-impedance amplifier in the front-end electronics not only converts current to voltage but also provides a negative damping effect for the MEMS sensor. In MEMS capacitive sensors, damping occurs due to factors such as energy dissipation, viscous resistance, material losses, etc. [27]. The amplifier produces negative damping to cancel out the existing damping in the sensor. AGC adjusts the gain of the amplifier for a consistent oscillation amplitude and eliminates the damping effect. This allows the sensor to function as a mass-spring system in self-resonance.

In the ZI Lock-in Amplifier, AGC compares the reference amplitude used to drive the sensor with the demodulated sensor output amplitude [29]. The AGC adjusts the amplitude until the user-specified desired amplitude or gain is reached. Both PLL and AGC control loops are applied to the demodulated signal output to allow the sensor to operate in self-resonance without being affected by frequency shift due to temperature and also improve the stability of the output signal [30].

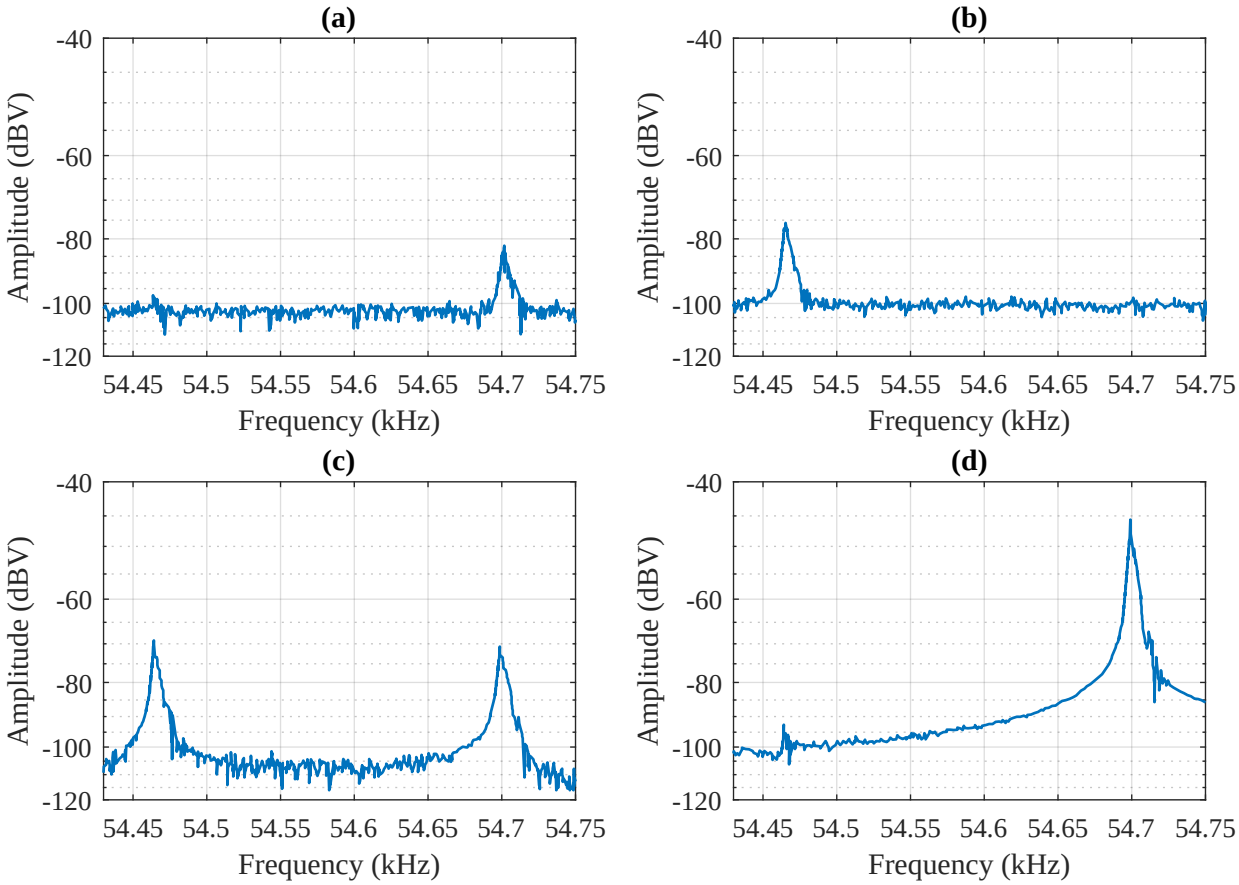

Figure 3.8: Measured Frequency Sweeps for TRG Device (a) Drive at X-axis, detect at X-axis (b) Drive at X-axis, detect at Y-axis (c) Drive at Y-axis, detect at X-axis (d) Drive at Y-axis, detect at Y-axis

3.3 Experimental Results

Based on the frequency sweep results from driving at the x-axis (Fig. 3.8 a-b) and the y-axis (Fig. 3.8 c-d), a frequency split was observed in both the x-axis and y-axis when driving on only one axis. Ideally, when no rotation is applied to the sensor and with a perfectly symmetrical ring structure that includes a 45-degree offset for the wineglass mode, the displacement of the ring in the y-axis—assuming driving in the x-axis—should be minimal or close to zero. In other words, the frequency split of the sensor should also be zero. However, in real-world applications, fabrication at a small scale may introduce slight imperfections in the ring's shape, which can alter the resonant frequency on the x-axis and y-axis. This

Resonant Frequency 1	54.465 kHz
Resonant Frequency 2	54.700 kHz
Frequency Split	245 Hz
Quality Factor 1	117k
Quality Factor 2	120k

Table 3.1: Experimental Characterization Result of the Epi-Seal TRG

imperfection leads to "crosstalk" where a certain amount of vibration energy leaks to the y-axis vibration due to shape asymmetry, causing a frequency split observed in the plots [30].

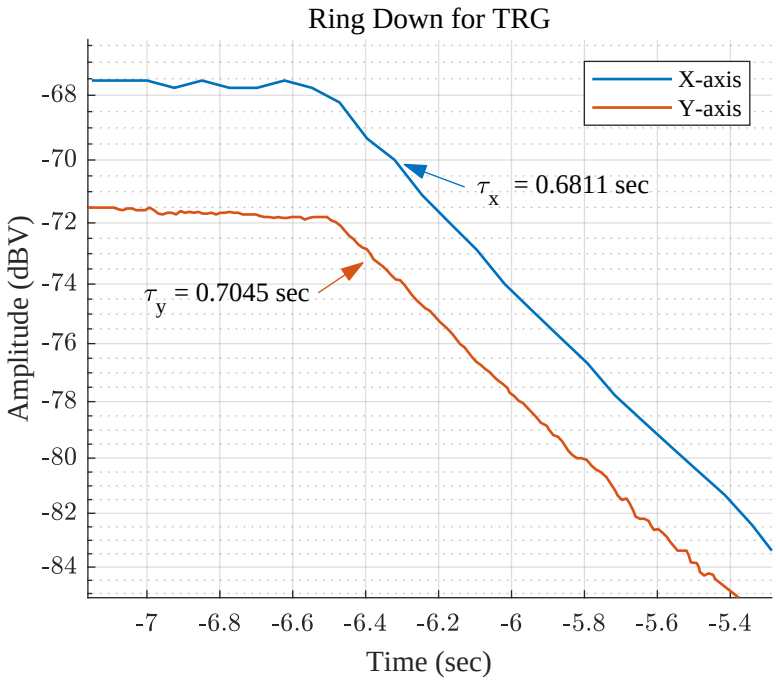

Figure 3.9: TRG Ring-down time measurements for both X and Y axis for quality factor estimation

The quality factors were estimated using the ring-down method, with the PLL locked at the measured resonance driving frequency for the X and Y-axes. This method involves pausing the external AC driving signals to allow the vibrations of the TRG to decay [31]. 3.9 displays the ring-down time measurements for both axes. The ring-down time constants τ were determined by measuring the time difference in seconds from the initial amplitude and the point where the decayed amplitude reaches 1/e of the initial value [32]. The quality

factor can be estimated using the following equation:

$$Q = \pi \cdot f_0 \cdot \tau \tag{3.1}$$

where f_0 is the measured resonant frequency. Using eq 3.1, the quality factor and ring-down time constant for the X-axis and Y-axis of the TRG were estimated to be 117k and 120k, with 0.6811 s and 0.7045 s, respectively.

3.4 Conclusion

This chapter presented a demonstration of a basic characterization using the EAM technique on an Epi-Seal Toroidal Ring Gyroscope (TRG). The measurements revealed a peak at 54.46 kHz on the X-axis and at 54.7 kHz on the Y-axis, with the frequency split measured at 241 Hz. A ring-down experiment was conducted with the PLL locked onto the AC driving signal, yielding a quality factor of 117k and 120k. Tuning can be achieved by applying a DC voltage on the tuning electrodes to further determine the scale factor and the bias instability of the TRG.

Chapter 4

High Quality Factor Frequency-Modulated Accelerometer

Building upon previous chapter's EAM method of extracting the natural frequency and quality factor for the TRG, this chapter focuses on the Frequency-modulated (FM) accelerometer. FM accelerometer adapts a classic MEMS capacitive structure based on a mass-spring-damper system. The working principle of the FM accelerometer is first discussed. Using a similar approach in TRG, the resonance frequency and the quality factor of the device are measured. Follow up with scale factor measurements and Allan deviation analysis to fully characterize the sensor performance.

4.1 Introduction

Compared with commercial MEMS accelerometers, frequency-modulated (FM) accelerometers have several advantages. In terms of vacuum packaging, FM accelerometers can achieve similar vacuum packaging requirements that could match Coriolis vibrating gyro-

scopes, which could be assembled with gyroscopes and form an IMU device on the same chip [33]. The resolution and dynamic range of the sensor are at least 3 orders higher than the amplitude-modulated accelerometers. However, one drawback of the frequency-modulated device is the frequency drift, which changes the performance of the sensor at various temperatures [3]. The detected sensor measurement at different temperatures could lead to huge differences in frequency due to material properties depending on the temperature coefficient of frequency. The device has two accelerometers created on the same die to resolve the issue of frequency drift from the change in material properties. This paper [34] experimentally demonstrated the capability of differential accelerometers as a temperature sensor and an accelerometer. The temperature-induced frequency shift can be mitigated using two identical accelerometers that experience the same geometric changes due to thermal expansion. The difference between their frequency outputs cancels out the common-mode frequency shift and reduces other background noise, resulting in more accurate measurements. Temperature can also be detected from the sum of both accelerometers' frequency outputs as the combined frequency shift increases linearly with temperature.

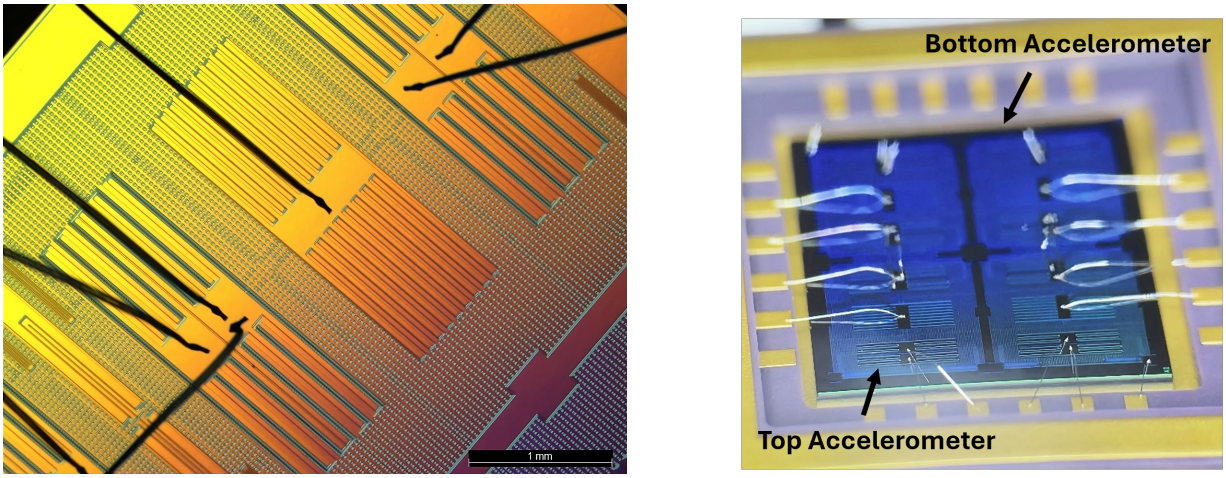

(a) FM Accelerometer taken using Leica Microscope

(b) Picture of FM accelerometer wire bonded to the DIP package

Figure 4.1: Pictures of the FM accelerometers

4.2 Working Principle

4.2.1 System Dynamics

The FM accelerometer can be simplified to a mass-spring system, similar to Fig. 4.2. The model features two masses and three springs connected in series. Two identical proof masses are connected by two springs k_1 on the side. An additional spring k_2 with a higher stiffness is positioned between the masses. The mass-spring system exhibits two degrees of freedom: in-phase and anti-phase. When the system is excited in in-phase, both masses move in the same direction. The higher stiffness k_2 spring moves along with the masses and remains nearly rigid. The system can be further simplified into a single mass connected to a single spring system, assuming both masses and k_1 springs are identical. The resonance frequency response of the system can be represented below:

$$\omega = \sqrt{\frac{k_1}{m}} \tag{4.1}$$

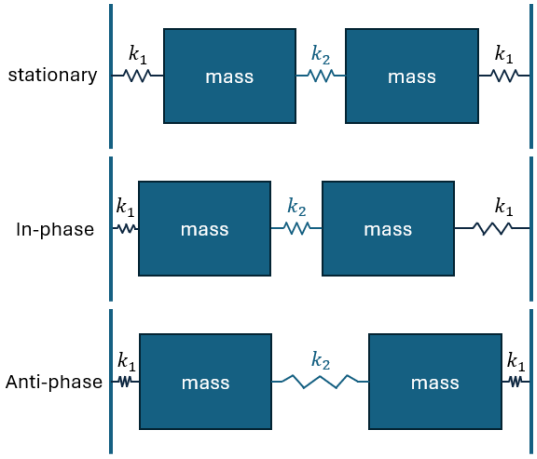

Figure 4.2: Schematics of an FM accelerometer with two identical masses connected with spring on a fixed side, with an additional spring placed between both masses

In anti-phase motion, the two masses move in opposite directions with the same amplitude. The center spring k_2 suffers higher compression and tension. The resonance frequency is

higher compared to the in-phase mode, with more restoring force exerted on the k_2 spring. The resonance frequency response of the system can be simplified to:

$$\omega = \sqrt{\frac{k_1 + 2k_2}{m}} \tag{4.2}$$

4.2.2 Device Features

Two main types of capacitive electrodes were used in the FM accelerometer design: comb drives and parallel plates, as shown in Fig. 4.3. The distance between the stationary and movable electrodes provides a fixed capacitance value:

$$C = \frac{\epsilon(wt)}{d} \tag{4.3}$$

where ϵ is the permittivity of free space, w is the width of the comb finger, t is the thickness of the comb finger, and d is the gap between the overlapping electrodes. Differential comb drives were used for actuation in the outer region and detection in the inner region of the device. The distance or the gap between the stationary and movable combs can influence the capacitance value. When an electrostatic force is applied or detected from the stationary comb drives, the capacitance change for the comb drives can be derived as:

$$\frac{dC}{dx} = \frac{\epsilon t}{d} \tag{4.4}$$

The parallel plates are located at the center of the proof mass, and they are mainly used for frequency tuning. DC voltage is applied to the parallel plate and introduces a negative spring stiffness in addition to the mechanical springs within the system. The capacitance

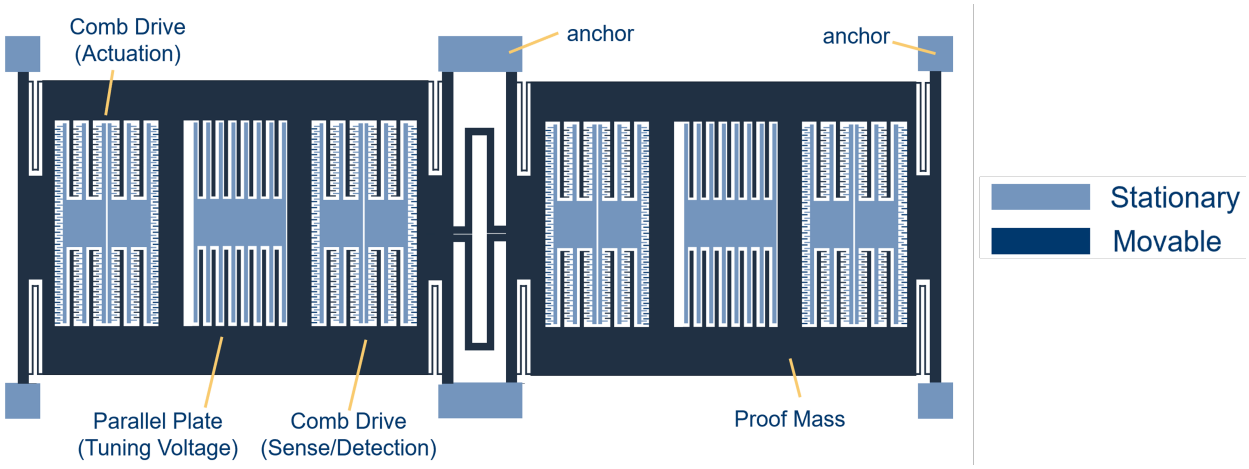

(a)

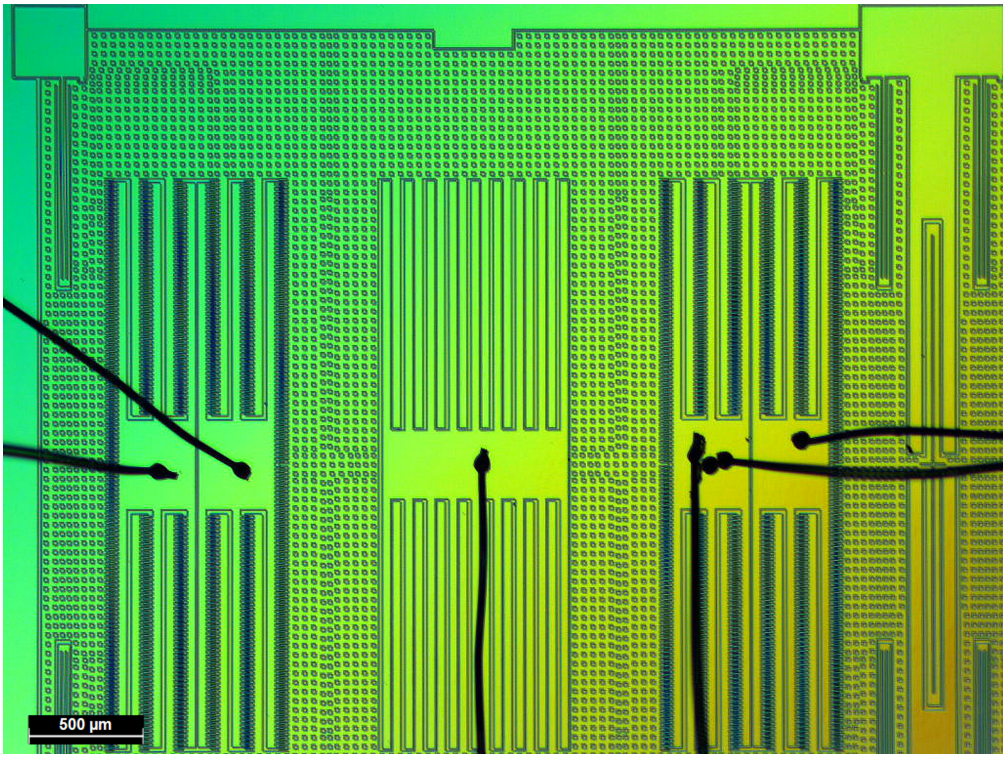

(b)

Figure 4.3: (a) Schematics of the Top FM accelerometer (b) Picture of the top FM accelerometer with wire bonded to its stationary electrodes

changes and the negative spring stiffness from the parallel plates are shown below:

$$\frac{dC}{dx} = \frac{\epsilon t w}{(d+x)^3} \qquad\qquad k_{\text{electrical}} = \frac{\epsilon A V^2}{d^3} \tag{4.5}$$

where A is the area of the overlapping area for the parallel plates. The electrodes are fixed to the substrate, while the proof masses with etch holes are suspended by the serpentine springs on the side. A double-ended tuning fork (DETF) is used as the center spring that links to the proof mass. The DETF resonator offers perks like high sensitivity with low energy loss and high stability with temperature fluctuations [35]. It is commonly known to be used in capacitive resonant accelerometers with frequency readout [20]. Based on the structure of the device, the equation of motion of the device can be written as [34]:

$$m\ddot{x} + c\dot{x} + \left(k_{\text{mechanical}} - \frac{\epsilon_0 A V^2}{\left(d_0 + \frac{ma}{k}\right)^3} \right) x = a \tag{4.6}$$

where m is the proof mass, d_0 is the initial gap distance of the parallel plates, k is the mechanical spring stiffness, and a is the acceleration applied to the sensor. The effective spring stiffness is a combination of mechanical and negative stiffness from parallel plates. Fig. 4.1b presented a close-up picture of the device with a top and a bottom accelerometer (Accelerometer 1 and Accelerometer 2). Two accelerometers were used in the configuration for accurate measurements and to mitigate the effects of temperature on silicon. FM accelerometers are fabricated using the conventional silicon-on-insulator (SOI) method. Silicon material is used as the main structure of the device. Due to its material properties, temperature changes cause thermal expansion to alter the device dimension and resulting in a shift in natural frequency. The dual accelerometer configuration significantly reduces the impact of thermal expansion and maintains measurement stability.

Using the EAM technique and differential detection reduces the impact of parasitic feedthrough signals on MEMS sensor reading. EAM shifts the motional signal of the sensor to

a higher-frequency region by mixing it with a high-frequency carrier signal. Demodulation and proper filtering can reconstruct the motional signal with no parasitic capacitance in the lower frequency region. The FM accelerometer has symmetrical-shape electrodes and proof masses with a DETF resonator located at the center to drive the sensor in anti-phase. The sensor structure allows for differential detection and actuation by measuring the difference in capacitance changes between two identical electrodes. Noise and parasitic capacitance equally affect the detection electrodes sensing in opposite driving directions. This results in common-mode cancellation that reduces these unwanted signals, including parasitic capacitance. The combination of EAM and differential detection significantly improves and sharpens the motional sensor output.

4.3 Experimental Results

The instrumentation setup for the FM accelerometer is similar to the TRG setup except for the signal connections. Signal Input 1 is connected to the top accelerometer, and Signal Input 2 is connected to the bottom accelerometer. The outer sides of the proof masses are used for excitation to drive the accelerometer in anti-phase. The detection electrodes located on the inner sides of the proof masses generate a differential signal of the sensor movement. The differential signal goes through two trans-impedance amplifiers to convert a current signal into a voltage signal. After converting to the voltage signal, the differential signal is routed to the instrumentation amplifier to reject the differential signals in common and filter out possible noise. A pre-determined resistor is selected for the gain output which is then used for further processing in the ZI Lock-In Amplifier.

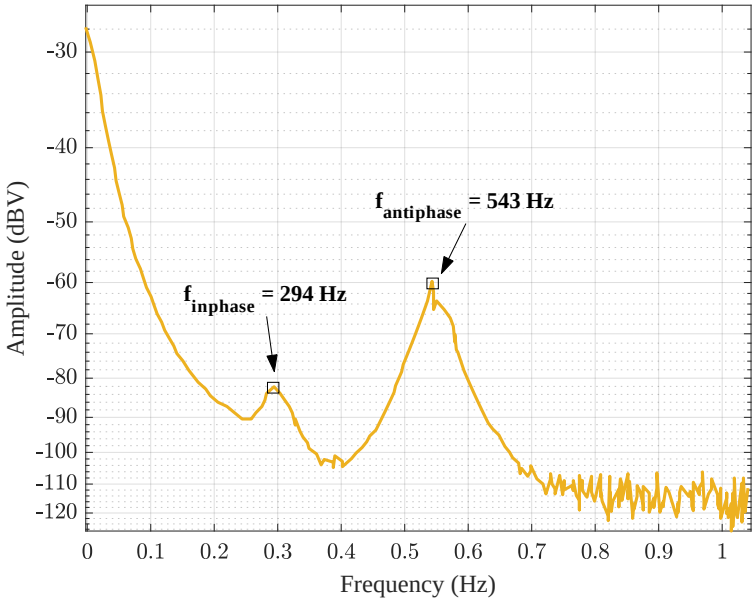

Figure 4.4: Frequency Sweep of the FM Accelerometer indicating the in-phase frequency and the anti-phase frequency

4.3.1 Resonance Frequency and Quality Factor

A carrier signal with an amplitude of 500 mV at 52 kHz is applied to the anchor, and a DC bias signal of 10 mV is merged with the AC driving signal of 200 mV at the detected resonance frequency from the frequency sweep. The experimental frequency sweep for the top accelerometer is shown in Fig. 4.4, with an in-phase frequency of 294 Hz and an anti-phase frequency of 543 Hz for the top accelerometer. Another frequency sweep was conducted for the bottom accelerometer, with an anti-phase frequency of 564 Hz. The top and bottom accelerometers have a frequency difference of 20 Hz. This discrepancy can be minimized by applying an appropriate tuning voltage through the parallel plate electrodes.

Ring-down experiments were performed on both accelerometers, with measurements taken simultaneously using a carrier signal. The ring-down time constant for both devices was estimated at 9 minutes, as shown in Fig. 4.5. The top accelerometer has a slightly higher quality factor compared with the bottom one, with a value of 950k and 951k. Compared to a device with a similar structure with a resonance frequency of 2.2 kHz, the quality factor was

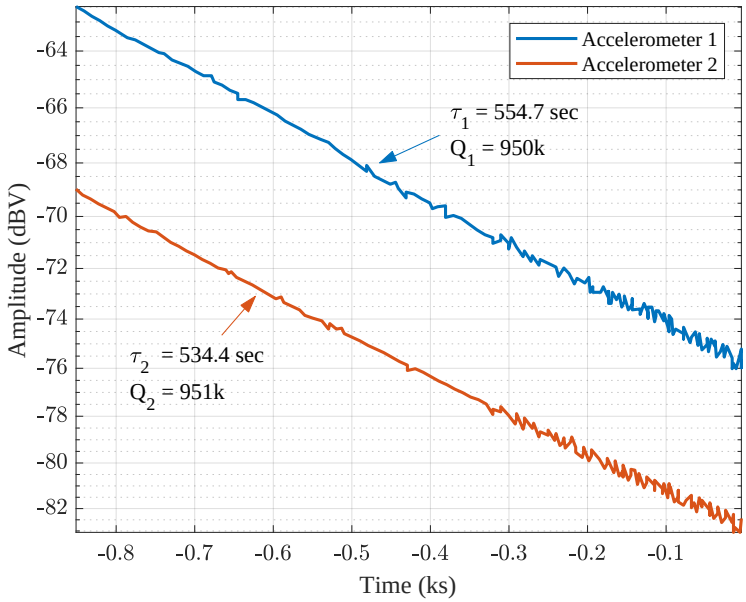

Figure 4.5: Ring Down Time measurement of the FM Accelerometers

achieved at 2.1M [34]. Unlike the Epi-seal device, FM accelerometers were vacuum sealed with getter materials. Getters material is used to preserve a near-perfect vacuum condition for the sensor to reach a high-quality factor [36]. Even after more than a decade of vacuum-sealing with getter material, the device remarkably maintains an impressive quality factor of nearly 1M.

4.3.2 Scale Factor and Bias Instability

The measurement of the scale factor and noise parameters of the FM accelerometer were taken with another unit with half the sensitivity of the one presented earlier. Scale factors were obtained using a manual tilt and turn table and perform a 2 g tip-over test. The test setup is shown in Fig. 4.6, with the device tilted from -90 degrees to +90 degrees, corresponding to the g-force due to gravity. The scale factor plot for both accelerometers is also illustrated in Fig. 4.6. The scale factor was measured in voltage instead of the shift in resonant frequency. The displacement of the proof mass is being measured for the output as the voltage for AM devices. The input is taken in voltage, and the output is g in acceleration.

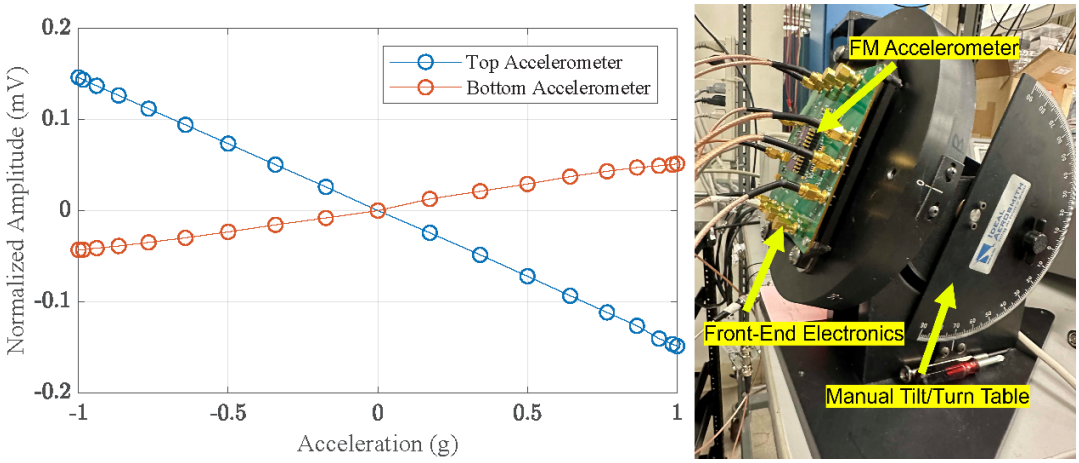

Figure 4.6: Scale Factor Measurement of both FM Accelerometers (Left) Scale Factor Experimental Setup on a manual tilt/turn table (Right)

From the normalized scale factor, acceleration can be converted using the following equation [37]:

$$y = (SF \cdot x) + B \tag{4.7}$$

where SF is the scale factor unit in mV/g, x is the acceleration in g, y is the output voltage amplitude of the sensor in mV, and B is the offset of the measurements. The scale factors of 0.14 mV/g and 0.049 mV/g were measured for accelerometer 1 and accelerometer 2, respectively. Accelerometer 1 is more sensitive than accelerometer 2 with a higher voltage change per g-force acceleration. The scale factor can be tuned and increased by applying a tuning voltage through the parallel plates.

Allan deviation analysis was conducted to understand the stability and noise performance of the sensor [38]. The device was placed in an environment with an uncontrolled temperature and slight external disturbances. A ZI lock-in amplifier was used to collect the voltage output amplitudes from both accelerometers at a sampling rate of 112.4 Hz sampling rate for over 9.5 hours. The converted differential output amplitude in mg over 9.5 hours of data is shown in Fig. 4.7a. The in-run bias instability and velocity random walk (VRW) can be estimated

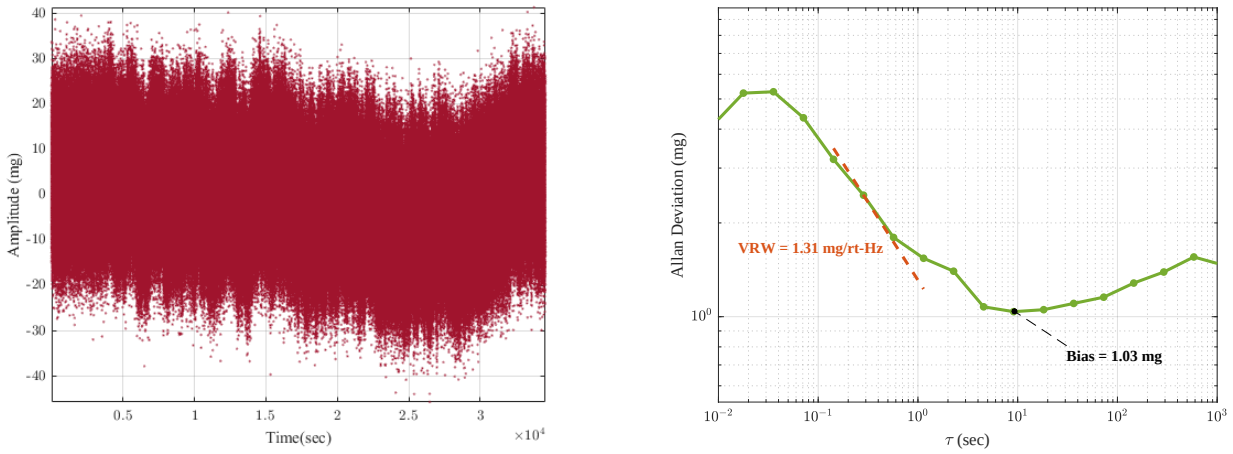

(a) (b)

Figure 4.7: (a) Stationary differential measurements for 9.5 hours (b) Allan deviation plot of the differential measurements in uncontrolled temperature environment

from the slope at 0 and slope at -0.5 region on the Allan deviation plot. Fig. 4.7b is the Allan deviation plot for the FM accelerometers on a log-log scale. A -0.5 slope was fitted on the plot, and the VRW was calculated at 1.31 $\frac{\text{mg}}{\sqrt{\text{Hz}}}$. The bias instability was computed at 1.03 mg from the zero-slope region of the plot. The bias value can be affected by temperature fluctuation and other external factors [38]. It is expected that the bias instability can be reduced with a test setup in a temperature-controlled and minimal-vibration environment.

4.4 Conclusion

The FM accelerometers were experimentally tested with the top and the bottom accelerometers, which were vacuum-sealed using getter material in the DIP package. From the frequency sweep, an anti-phase resonance frequency of 544 Hz for the top accelerometer and 564 Hz for the bottom accelerometer were obtained. Both devices have a high-quality factor of approximately 950k, with a ring-down time constant of around 9 minutes. The FM accelerometer demonstrated the capability of functioning as an AM accelerometer with changes in output voltage to represent acceleration. A 2 g tip-over test is conducted to obtain the scale factor

values, with the top and bottom accelerometers measured at 0.14 mV/g and 0.05 mV/g, respectively. The bias instability was computed at 1.03 mg, and the velocity random walk is 1.31 $\frac{\text{mg}}{\sqrt{\text{Hz}}}$. Compared to the FM accelerometer operating in FM mode, the VRW value is five times higher than in AM mode. This demonstrates the device is capable of operating in both modes, with the FM mode having a slightly better performance advantage, including better SNR reading and greater resilience to voltage stability issues that exist in the AM mode.

Chapter 5

Conclusion

This thesis focuses on the use of Electromechanical Amplitude Modulation (EAM) to remove feed-through parasitic capacitance in MEMS capacitance resonance inertial sensors. The research demonstrated the effectiveness of EAM with experimental validation from an Epi-Seal Toroidal Ring Gyroscope (TRG) and Frequency-Modulated (FM) Accelerometer. The key conclusions from each chapter are summarized below:

- Chapter 2: Electromechanical Amplitude Modulation

  The background and working principle of the EAM technique were explained using radio frequency (RF) terminology to mitigate parasitic capacitance. Signal mixing and filtering of both the AC driving signal and carrier signal reconstructed the motional sensor output without noise and parasitic capacitance. Theoretical Simulink simulation and experimental results verified the modulation and demodulation processes of EAM to extract the motional signal of the sensor.

- Chapter 3: Toroidal Ring Gyroscope (TRG)

  The Toroidal Ring Gyroscope was characterized using the EAM technique. The difference in resonance frequency between the drive and sense axes indicated a shape

imperfection from fabrication. The quality factor was also extracted from the device which indicates the energy dissipation and resolution of the sensor.

- Chapter 4: High-Quality Factor Frequency-Modulated Accelerometer

  The performance of the FM accelerometer was assessed in Amplitude Modulation (AM) mode by detecting changes in voltage amplitude by driving the device at its resonance frequency. Key parameters were extracted, including the resonance frequency, quality factor, sensitivity, and noise parameters from the Allan deviation analysis. This chapter confirmed that EAM could accurately extract the actual sensor signal output. The performance of the sensor can be further improved in a controlled environment.

This thesis demonstrated the benefits of using the Electromechanical Amplitude Modulation (EAM) technique and filtering in MEMS inertial sensors. It revealed the capability to extract the motional sensor signal output free from parasitic capacitance and reduce background noise. Future work will focus on enhancing sensor readings by applying tuning voltage to the sensor to improve sensor performance.

Bibliography

[1] Shuzheng Shi, Liyong Ma, Kai Kang, Jie Zhu, Jinjiang Hu, Hong Ma, Yongjun Pang, and Zhanying Wang. High-sensitivity piezoelectric mems accelerometer for vector hydrophones. *Micromachines*, 14(8), 2023.

[2] Yunbo Shi, Yongqi Zhao, Hengzhen Feng, Huiliang Cao, Jun Tang, Jie Li, Rui Zhao, and Jun Liu. Design, fabrication and calibration of a high-g mems accelerometer. *Sensors and Actuators A: Physical*, 279:733–742, 2018.

[3] Jiangbo He, Wu Zhou, Huijun Yu, Xiaoping He, and Peng Peng. Structural designing of a mems capacitive accelerometer for low temperature coefficient and high linearity. *Sensors*, 18(2), 2018.

[4] Michael Haub, Martin Bogner, Thomas Guenther, André Zimmermann, and Hermann Sandmaier. Development and proof of concept of a miniaturized mems quantum tunneling accelerometer based on ptc tips by focused ion beam 3d nano-patterning. *Sensors*, 21(11), 2021.

[5] Chenguang Xin, Zhongyao Zhang, Xuhu Wang, Changjiang Fan, and Mengwei Li. Ultracompact single-layer optical mems accelerometer based on evanescent coupling through silicon nanowaveguides. *Scientific Reports*, 12(1):21697, 2022.

[6] D. Senkal, S. Askari, M. J. Ahamed, E. J. Ng, V. Hong, Y. Yang, C. H. Ahn, T. W. Kenny, and A. M. Shkel. 100k q-factor toroidal ring gyroscope implemented in wafer-level epitaxial silicon encapsulation process. In *2014 IEEE 27th International Conference on Micro Electro Mechanical Systems (MEMS)*, pages 24–27, 2014.

[7] Alexandra Efimovskaya, Yu-Wei Lin, and Andrei M. Shkel. Double-sided process for mems soi sensors with deep vertical thru-wafer interconnects. *Journal of Microelectromechanical Systems*, 27(2):239–249, 2018.

[8] N. Yazdi, F. Ayazi, and K. Najafi. Micromachined inertial sensors. *Proceedings of the IEEE*, 86:1640–1659, 1998.

[9] Zakriya Mohammed, Ibrahim (Abe) M Elfadel, and Mahmoud Rasras. Monolithic multi degree of freedom (mdof) capacitive mems accelerometers. *Micromachines*, 9(11):602, 2018.

[10] Yi Chiu, Cheng-Yen Lin, and Hao-Chiao Hong. A monolithic cmos-mems reconfigurable/tunable capacitive accelerometer with integrated sensing circuits. *Frontiers in Mechanical Engineering*, 8:876714, 2022.

[11] Dongliang Chen, Liang Yin, Qiang Fu, Yufeng Zhang, and Xiaowei Liu. Measuring and calibrating of the parasitic mismatch in mems accelerometer based on harmonic distortion self-test. *Sensors and Actuators A: Physical*, 313:112159, 2020.

[12] Eurico Esteves Moreira, Burkhard Kuhlmann, Filipe Serra Alves, Rosana Alves Dias, Jorge Cabral, João Gaspar, and Luis Alexandre Rocha. Highly sensitive mems frequency modulated accelerometer with small footprint. *Sensors and Actuators A: Physical*, 307:112005, 2020.

[13] J. Jalil, Y. Ruan, and Y. Zhu. Room-temperature sensing of single electrons using vibrating-reed electrometer in silicon-on-glass technology. *IEEE Electron Device Letters*, 39(12):1928–1931, 2018.

[14] Xianshan Dong, Shaohua Yang, Junhua Zhu, Yunfei En, and Qinwen Huang. Method of measuring the mismatch of parasitic capacitance in mems accelerometer based on regulating electrostatic stiffness. *Micromachines*, 9(3):128, 2018.

[15] Clark T. Nguyen. *Micromechanical signal processors*. PhD thesis, UC Berkerly, 1994 1994.

[16] Andre Loch Gesing, Zargos Neves Masson, Diego Calero Arellano, Fabio Alves, Stephan Paul, and Julio Apolinario Cordioli. Middle ear ossicular chain vibration detection by means of an optimized mems piezoelectric accelerometer. *IEEE Sensors Journal*, 19(6):2079–2086, 2019.

[17] Xuewen Gong, Yu-Chun Kuo, Guodong Zhou, Wen-Jong Wu, and Wei-Hsin Liao. An aerosol deposition based mems piezoelectric accelerometer for low noise measurement. *Microsystems and Nanoengineering*, 9:23, 03 2023.

[18] N Chitra and J Grace Jency Gnanammal. A high performance mems piezoresistive accelerometer for pathological tremor diagnostic system. In *2016 3rd International Conference on Devices, Circuits and Systems (ICDCS)*, pages 157–160. IEEE, 2016.

[19] Feng Liu, Shiqiao Gao, Shaohua Niu, Yan Zhang, Yanwei Guan, Chunhui Gao, and Ping Li. Optimal design of high-g mems piezoresistive accelerometer based on timoshenko beam theory. *Microsystem Technologies*, 24:855–867, 2018.

[20] Chen Wang, Fang Chen, Yuan Wang, Sina Sadeghpour, Chenxi Wang, Mathieu Baijot, Rui Esteves, Chun Zhao, Jian Bai, Huafeng Liu, and Michael Kraft. Micromachined accelerometers with sub-µg/hz noise floor: A review. *Sensors*, 20(14), 2020.

[21] Qianbo Lu, Jian Bai, Kaiwei Wang, and Sailing He. Design, optimization, and realization of a high-performance moems accelerometer from a double-device-layer soi wafer. *Journal of Microelectromechanical Systems*, 26(4):859–869, 2017.

[22] Dominique Fourguette, Volkan Ötügen, Liane M Larocque, Greg A Ritter, Tindaro Ioppolo, and Darren Hart. Optical mems-based seismometer. *Proceedings of the 2011 Monitoring Research Review: Ground-Based Nuclear Explosion Monitoring Technologies, Portsmouth, Virginia*, pages 23–25, 2008.

[23] Alexandra Efimovskaya. *Multi-Axis Solutions for MEMS Inertial Sensors*. PhD thesis, UC Irvine, 2017.

[24] A.M. Shkel. Type i and type ii micromachined vibratory gyroscopes. In *2006 IEEE/ION Position, Location, And Navigation Symposium*, pages 586–593, 2006.

[25] Yusheng Wang, Yu-Wei Lin, Janna Rodriguez, Gabrielle D Vukasin, Dongsuk D Shin, Hyun-Keun Kwon, David B Heinz, Yunhan Chen, Dustin D Gerrard, Thomas W Kenny, et al. On decoupled quantification of energy dissipation mechanisms in toroidal ring gyroscopes. In *Solid-State, Actuat., Microsyst. Workshop Tech. Dig.*, pages 318–321, 2018.

[26] Yunhan Chen, Ian Flader, Dongsuk Shin, C.H. Ahn, Janna Rodriguez, and Thomas Kenny. Robust method of fabricating epitaxially encapsulated mems devices with large gaps. *Journal of Microelectromechanical Systems*, PP:1–9;, 10 2017.

[27] Doruk Senkal and A.M. Shkel. *Whole-Angle MEMS Gyroscopes: Challenges and Opportunities*. IEEE Press with John Wiley and Sons, 05 2020.

[28] PLL Tab - HF2 User Manual.

[29] PID Tab - HF2 User Manual.

[30] Cenk Acar and Andrei Shkel. *MEMS vibratory gyroscopes: structural approaches to improve robustness*. Springer Science & Business Media, 2008.

[31] Romain Stomp. Ring-down method for rapid determination of high q-factor resonators, Dec 2020.

[32] James M. Lehto Miller, Azadeh Ansari, David B. Heinz, Yunhan Chen, Ian B. Flader, Dongsuk D. Shin, L. Guillermo Villanueva, and Thomas W. Kenny. Effective quality factor tuning mechanisms in micromechanical resonators. *Applied Physics Reviews*, 5(4):041307, 12 2018.

[33] U.S. Patent 9274136B2, Mar. 2016. Trusov, Alexander A. and Zotov, Sergei A. and Shkel, Andrei M.

[34] Sergei A. Zotov, Brenton R. Simon, Alexander A. Trusov, and Andrei M. Shkel. High quality factor resonant mems accelerometer with continuous thermal compensation. *IEEE Sensors Journal*, 15(9):5045–5052, 2015.

[35] Shirin Ghaffari, Eldwin Jiaqiang Ng, Chae Hyuck Ahn, Yushi Yang, Shasha Wang, Vu A. Hong, and Thomas W. Kenny. Accurate modeling of quality factor behavior of complex silicon mems resonators. *Journal of Microelectromechanical Systems*, 24(2):276–288, 2015.

[36] Adam R Schofield, Alexander A Trusov, and Andrei M Shkel. Versatile vacuum packaging for experimental study of resonant mems. In *2010 IEEE 23rd International Conference on Micro Electro Mechanical Systems (MEMS)*, pages 516–519. IEEE, 2010.

[37] Brenton Ross Simon. *Mode ordering in anti-phase driven MEMS gyroscopes and accelerometers*. University of California, Irvine, 2014.

[38] Tobias Hiller, Miloš Vujadinović, Lukas Blocher, Wolfram Mayer, Dušan Radović, Thorsten Balslink, Thomas Northemann, and Alexander Buhmann. Practical approaches to allan deviation analysis of low-cost mems inertial sensors. In *2023 IEEE International Symposium on Inertial Sensors and Systems (INERTIAL)*, pages 1–4, 2023.

[39] Eudald Sangenis Rafart. *Enhancing Situational Awareness for Firefighters by Blending Sensing Modalities*. PhD thesis, UC Irvine, 2023.

[40] Sina Askari. *Calibration Decision System of MEMS Gyroscope for Bio-Inertial Application*. PhD thesis, UC Irvine, 2019.

Appendix A

NEVERLOST - Handheld Platform Design

This appendix provides a summary of the NEVERLOST handheld platform design iterations and features.

A.1 Introduction

This side project highlights the development of a customized, ergonomic handheld object localization platform for the NEVERLOST project [39]. It is used in conjunction with an augmented reality headset (Magic Leap 2 headset) and a foot-mounted IMU for hazard spotting and mapping purposes. The design of the handheld platform is inspired by and closely resembles commercial controllers like the Magic Leap 2 Controller.

The handheld platform consists of several sensors and electronics modules that are attached as a whole. Several buttons and triggers were designed for interaction, and power buttons were intended for future use in software development. The problem of the handheld platform

prototype is first analyzed, then the design ideas and design iterations are presented, and 3D printing issues are then discussed. Lastly, the conclusion and future work of the current model are addressed. This appendix does not include sensor fusion and algorithm for navigation but the design constraints, design considerations, and history of improved versions of the designed models.

A.2 Design Considerations

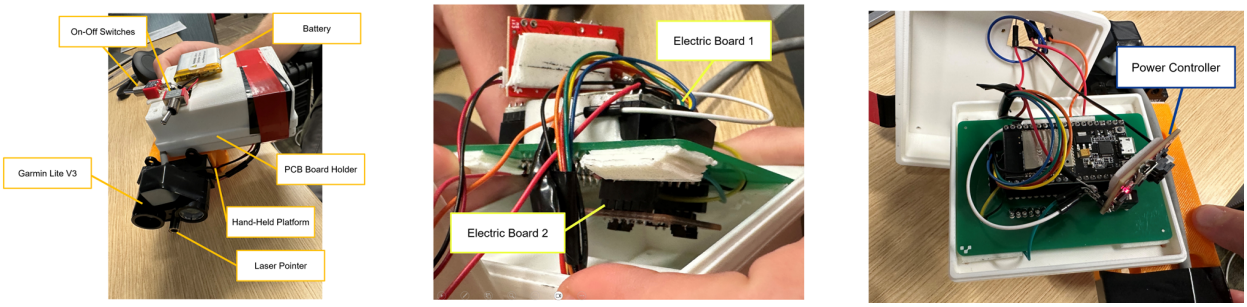

(a) Exterior (b) Interior - Top (c) Interior - Bottom

Figure A.1: Handheld Platform Prototype

The handheld platform prototype used for demo/testing with the Unity software had several notable issues. Most components were secured in place using duct tape, which is not a reliable and stable setup for the sensors and electronics module, as shown Fig. A.1. The wires were found tangled and loose inside the electronic holder, making it difficult to effectively adjust or perform further upgrades to the electronics hardware or prototype. The previous configuration also posed difficulties when switching and charging the replaceable battery, as all the components were barely secure. Additionally, the on-off toggles were hot-glued and protruded from the edge of the device. Most importantly, the overall design of the old temporary handheld platform is difficult to grip with parts duct-taped and randomly installed hardware and 3D printed components. The components include a VLM-520-73 dotted laser pointer, Garmin lite V3 for optical measurement sensor, two on-off switches for

electronics and laser, a 3D printed handle, a 3.7 V lithium-ion rechargeable battery, a power module, ICM 20948 IMU module, and a ESP 32 Wi-Fi/Bluetooth module.

The objective of the supported project is to design and manufacture an ergonomic handheld platform that has similar functionality and grip to the Magic Leap 2 controller. The handheld platform is intended to be used with the Magic Leap 2 headset with a QR code attached to the back for accurate positioning. The design must incorporate several essential functions. The design should have the on-off toggles placed near fingers for control and convenience. The electronics holder can be positioned underneath the handle, allowing for efficient and quick battery replacement. The wires need to be securely attached to the electronics holder. Sensors including laser and LiDAR should be pointed forward. The placement and orientation of other electronics are less important in the design. The ESP32 and the IMU module are permanently soldered onto the PCB board, and their configuration cannot be altered or detached.

A.3 Iterations

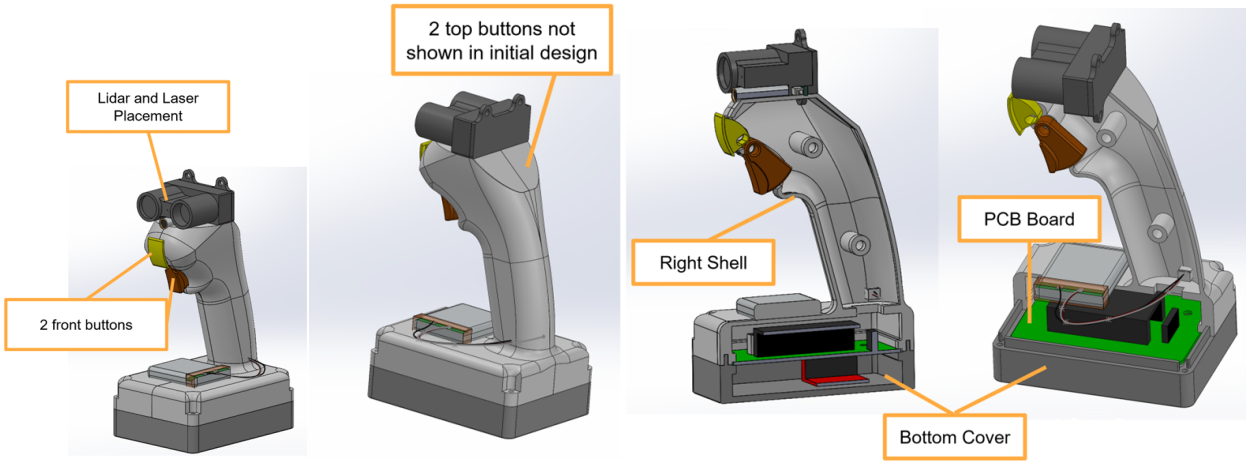

(a) Front View (b) Back View (c) Cross Sectional View

Figure A.2: Initial Handheld Platform Design

The initial design merges the structure form of the Magic Leap 2 Controller and Power drill with the blocky battery at the base, as shown in Fig. A.2. The controller has a bumper and a trigger button located in the front for easy access. The buttons are conveniently located on the index finger, while the rest of the fingers are wrapped around the handle. The LiDAR and laser are placed on the top of the controller and pointing forward. The battery is positioned on the top of the electronic holder for instant replacement. Since the electronic modules are permanently fixed on both sides of the PCB board, traditional screw fastening might damage the components. Instead, a secure alternative involves sandwiching the PCB on the sides to restrict movement and ensure stability in the handheld platform. A total of three bodies were 3D printed: the top left and top right bodies as the controller (light grey), and the bottom cover designed to hold the PCB (dark grey). The bottom cover can be screwed onto the top part of the controller.

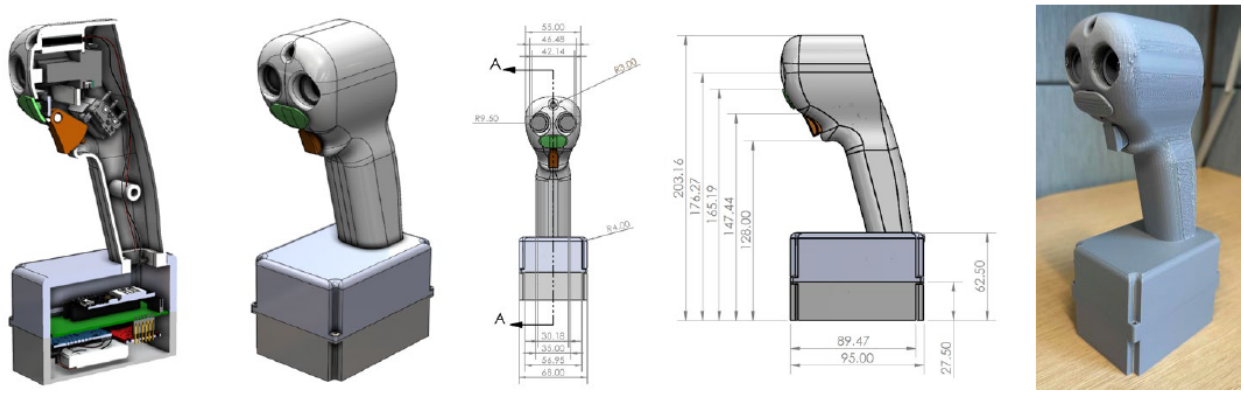

Figure A.3: Handheld Platform Version.4

A.4 3D printing Discussion

The exterior shell of the handheld platform is printed with a Mark forged Mark Two 3D printer. The printer is capable of printing carbon fiber as a reinforcement option and incorporating in the 3D printed part for higher strength. Two materials were tested and printed: Onyx and Precise-PLA. Onyx was tested and proven to be the best material to use for

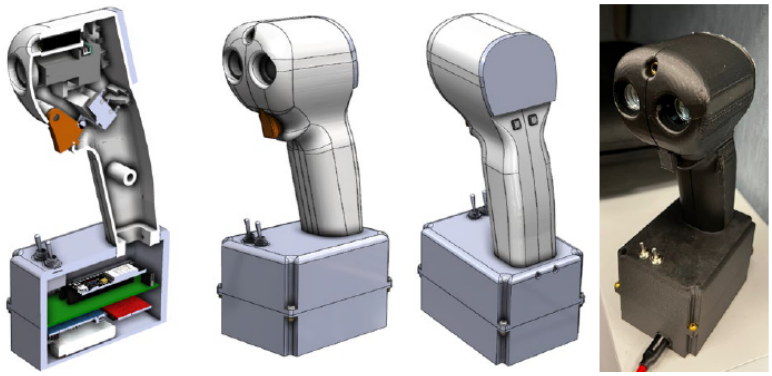

Figure A.4: handheld Platform Version.5

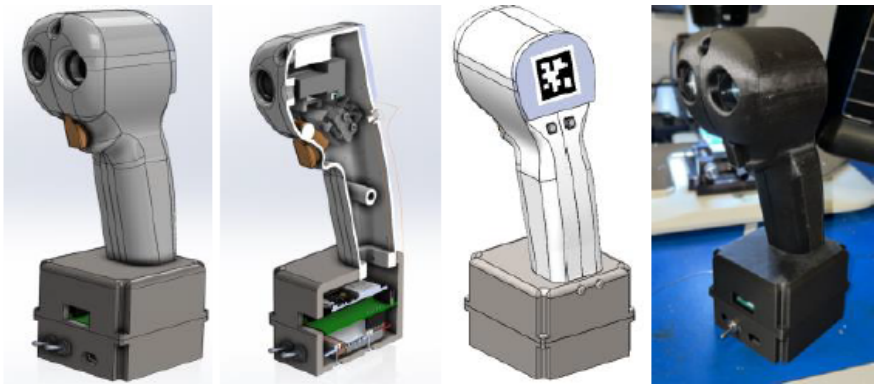

Figure A.5: Final version of the handheld platform

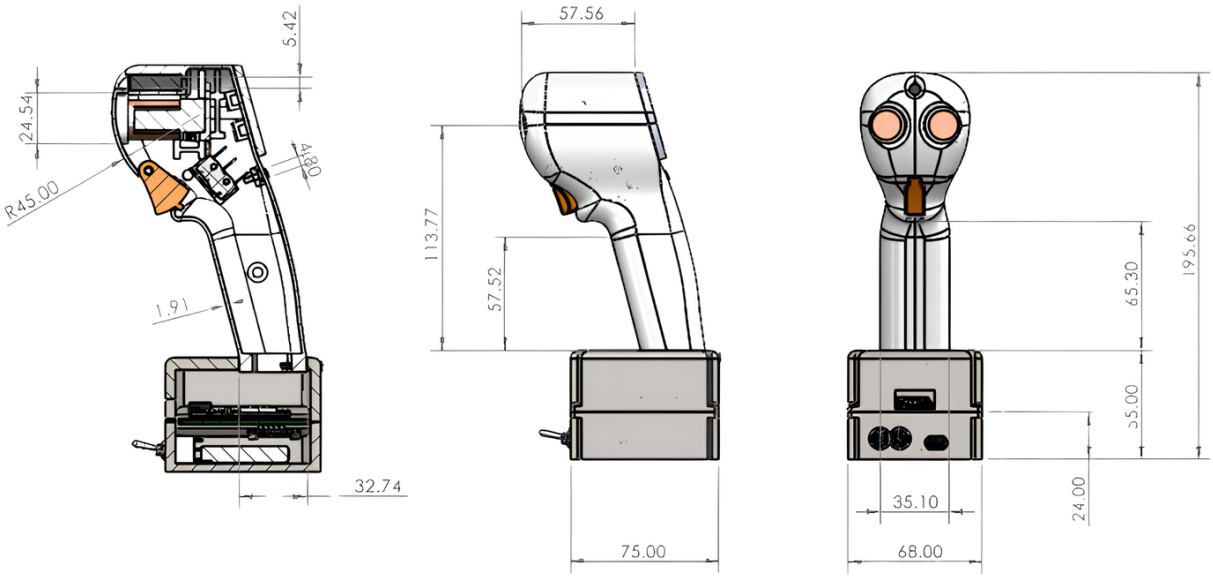

Figure A.6: Dimensions of the final version handheld platform with cross-sectional view

prototyping. It is a composite material with nylon and carbon fiber to make it stronger than the common PLA (polylactic acid) material used in 3D printing. The cost of onyx is about 1.5 times as expensive as the PLA and takes longer time to print. While Onyx takes longer to print, the support material removal difficulty, surface finish, strength, and flexibility of onyx still come out better than PLA in all aspects. However, several problems were encountered when printing with PLA material. The material properties of PLA warp and shrink quickly during cooling. Mark Two has no heated bed to prevent warping issues when removing finished printed parts. Printer head jam issues also existed on the average of every 4 prints. After every print, the purge rod maintenance and bed leveling take 2 to 3 hours. Fig. A.3 and A.4 present the difference between printing using Onyx versus P-PLA. The cost of manufacturing the bodies of the handheld platform ranges between $15 - $20 depending on the type of materials used and the volume printed. The entire handheld platform takes roughly a day to print the outer shell with Onyx. The Solidworks design must follow the design handbook of Mark Forged material for tolerance and clearance on free fitting and press fitting of some components.

A.5 Conclusion

Several versions of prototypes were designed and printed using P-PLA and Onyx material. P-PLA material was initially considered for prototyping due to its lower cost and faster printing time. The final and future parts will be printed using Onyx material for less downtime and maintenance needed on the printer compared with P-PLA material. The project is still ongoing, and plenty of features can be optimized on portability, compatibility, weight, ergonomics, mechanism design, and adding new functions like cameras. The plan for the next handheld platform will implement a wireless charging feature and a more compact design of the electronics holder at the base.

Appendix B

Zurich Instrument HF2LI Lock-In Amplifier - Gyroscope Operation

This Appendix chapter covers the features of the HF2LI Lock-In Amplifier from Zurich Instrument. The basic steps outlined in the following procedures are based on the principles of a TRG device. Similar documents and methodologies can be found in [37] and [40].

B.1 Test Setup

To demonstrate gyroscope operation, Epi-Seal TRG is selected and wire bonded to actuate in n = 2 mode for the gyroscope. Refer to Section 3.2 for proper configuration. A Vacuum chamber may be necessary if the testing device is not an Epi-Seal Device.

The following items are needed to perform gyroscope operation, the connection between the front-end electronics and Zurich Instrument is shown in Fig. 3.6:

- Zurich Instrument HF2LI Lock-In Amplifier
- Wire Bonded Gyroscope (TRG)
- Front-End Electronics (Top and Bottom PCB)
- BNC Cables
- Power Supplies
- LabOne Software (https://www.zhinst.com/americas/en/support/download-center)

B.2 LabOne User Interface Descriptions

Zurich Instrument might be difficult or overwhelming to use for first-time users. This section mainly discusses the features and settings necessary for the Gyro/Accel Operation. The Gyro/Accel Operations rely on a few essential tabs, such as the Lock-in Tab (HF2-MF Option), MOD Tab, Scope Tab, Plotter Tab, Sweeper Tab, and Spectrum Analyzer Tab, which will be discussed in detail. As illustrated in Fig. B.1, the Scope tab displays the signal inputs and outputs from the Zurich Instrument at the top, and the Lock-In Tab Options at the bottom.

B.2.1 Lock-In Tab

This tab serves as the main control center to showcase the parameters for signal inputs and generated signal outputs from the Zurich Instrument to adjust the frequency and amplitude of the signal outputs. In the signal input sections, the maximum voltage range can be adjusted by clicking on the auto-adjustment for better SNR inputs. It is important to note that the maximum allowable voltage range input into the Zurich Instrument is 2 Volts. Signal inputs can be either a differential input from the gyroscope, such as (positive and negative) pickoff/detected signals, or a signal output from the accelerometer, depending on

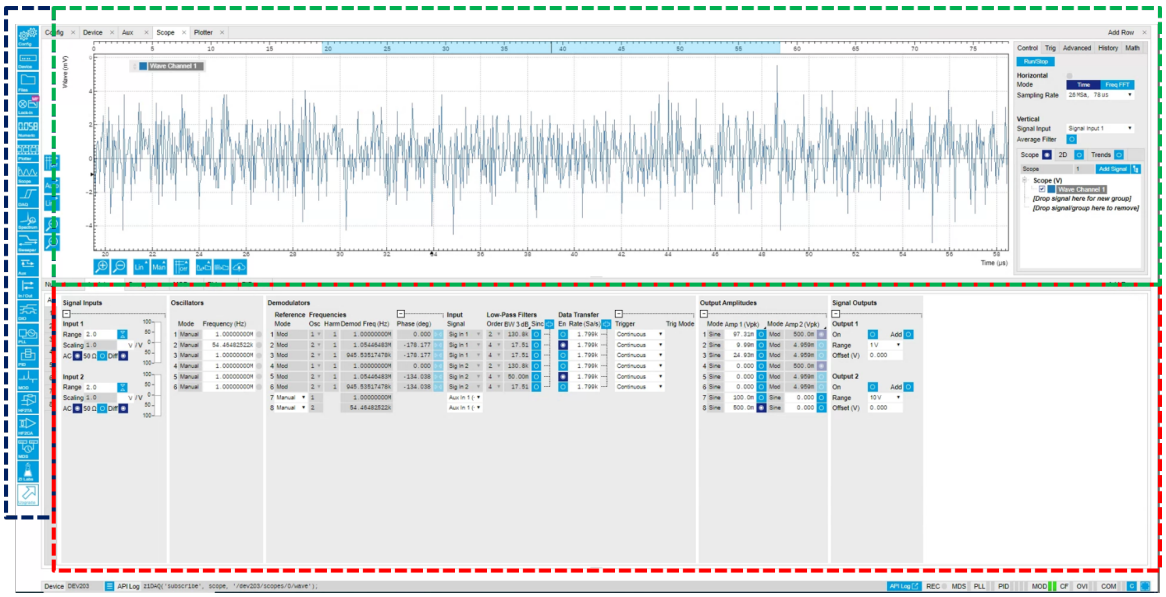

Figure B.1: Zurich Instrument LabOne User Interface with Scope Tab at the top and Lock-In tab at the bottom

the front-end electronic outputs. AC/DC coupling setting is recommended for turning on and removing the DC bias component from detected signals. The differential setting is enabled for gyroscopes that have a differential output connected to a Zurich instrument.

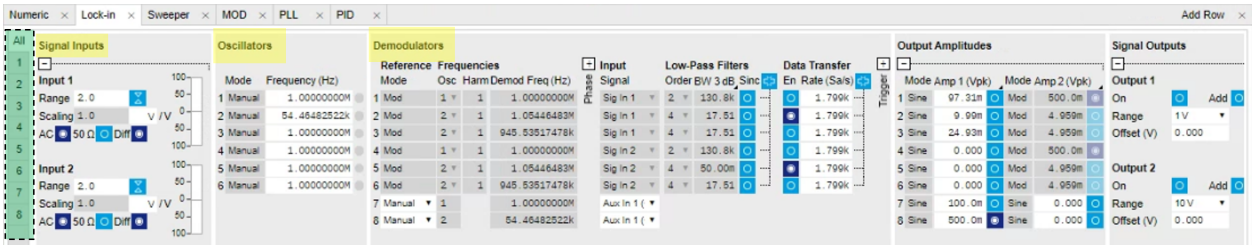

Figure B.2: LabOne Lock-In Tab

In the oscillator section, users can specify the oscillating frequency of the carrier signal and AC driving signal for the sensor. The default setting for all oscillators in the Zurich Instrument was 1 MHz. For instance, Fig. B.2 shows that oscillator 1 is set to be at 1Mhz for the carrier signal, and oscillator 2 is set to 54 kHz for the AC driving signal.

In the demodulator section, the demodulators display the parameters such as the modulation type (AM, FM, Manual), the oscillators used for demodulation, the mixed input signals and

reference signals, and the settings for low-pass filters. These values are shown in a greyed-out read-only format when modulation is activated. However, they can be altered under the Mod (Modulation) Tab, which is elaborated later in Section B.2.2.

Basic gyroscope/accelerometer operations rely on demodulators 1 through 3 for Signal Input 1, and demodulators 4 through 6 for Signal Input 2. Demodulators 7 and 8 are dedicated to phase-lock loop (PLL) and Automatic Gain Control (AGC). The demodulated frequency and amplitude values for demodulators 7 and 8 are adjusted based on the PID values and the desired frequency and amplitude to be adjusted, which can be modified under the PLL and PID Tab. Typically, data transfer is enabled for demodulators 1 and 4 for the demodulated carrier, and demodulators 4 and 5 for the sidebands (AC driving) from signal inputs 1 and 2. The data transfer rate is expressed in Samples Per Second (Sa/s), which indicates the frequency at which the samples are taken from continuous demodulated signals. When extracting data from the plotter tab, this sampling rate can be considered as a rate in Hz for future plotting.

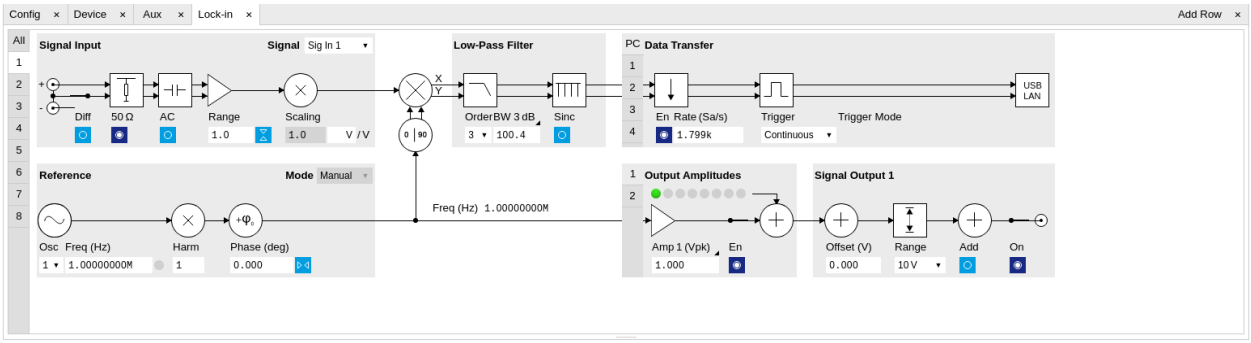

Figure B.3: LabOne Block Diagram of Demodulator 1

Each demodulator includes a block diagram view that offers a more comprehensive visual representation of the filter and signal mixing processes, from the signal inputs to the outputs as shown in Fig. B.3. The individual demodulator diagrams can be accessed through the green highlighted box on the right side, as depicted Fig. B.2. It is worth noting that the sinc feature is an optional setting that can filter out any harmonics in the demodulated outputs.

In the output amplitude section, "Mode Amp 1 (Vpk)" corresponds to the amplitude of the AC driving signal, and "Mode Amp 2 (Vpk)" corresponds to the amplitude of the carrier signal. It is recommended that the AC driving amplitude be set to either Demodulator 7 or 8. This arrangement allows the AGC to fine-tune the output voltage amplitude of the sensor to a desired level. In Fig. B.2, demodulator 7 was set to be used for the carrier frequency (oscillator 1), and demodulator 8 was set to be used for the AC driving frequency (oscillator 2). The carrier signal amplitude is read-only and must be set in the Mod Tab. For the carrier signal, demodulators 1 and 4 were activated and summed up to be 1V. For the AC signal amplitude, only Demodulator 8 was enabled at 500 mV.

In the signal output section, signal output 1 is for the AC driving signal, signal output 2 is for the carrier signal, and the toggle is on or off. To optimize signal quality, it is best to select the smallest voltage output range. As a preventive measure, it is crucial to turn off the signal outputs after each use of the Zurich Instrument. Failing to do so may result in the Zurich Instrument continuing output signals based on the last configuration, even if LabOne has been closed or exited.

B.2.2 Modulation Tab

The modulation by default is disabled and requires several adjustments to retrieve the demodulated signals from the sensor, as shown in Fig. B.4. Two main types of modulation can be selected: amplitude modulation (AM) and frequency modulation (FM), which are suitable for different sensor applications. Many in-house fabricated gyroscopes employ AM due to reliance on changes in the amplitudes of voltage. In applications like the Qual Mass Gyroscope (QMG) and FM Accelerometer, FM is used where the mode of detection is quasi-digital changes in frequency instead of the output voltage amplitude.

The modulation tab specifies the reference frequency required to demodulate both the carrier

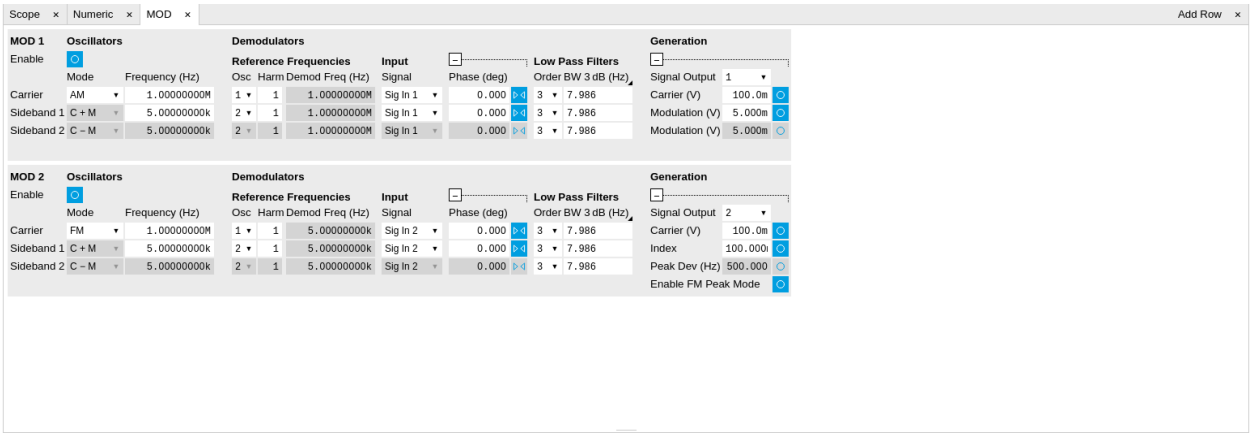

Figure B.4: LabOne Mod Tab with Modulation disabled for both modulators

and its sidebands. The reference frequency is adjustable under the oscillator frequency of the Lock-in Tab. The tab is organized into two sections, MOD 1 and MOD 2, corresponding respectively to signal inputs 1 and 2. Detailed information on the expected carrier signal and sidebands for each demodulator is presented in Table 1.

Zurich Instruments lock-in amplifiers feature built-in low-pass filters that eliminate high-frequency components from the demodulated signals. The Low-pass filter settings can be adjusted to optimize the SNR by tuning the filter order and bandwidth. Ideally, a lower filter order is preferable because it minimizes the signal delay and enhances the stability in feedback loops such as PLL and AGC. When dealing with a low demodulation frequency — taking the FM Accelerometer as an example — higher-order filters may be required to suppress the DC offset and reduce the influence of harmonics. In addition to the filter order, selecting the narrowest bandwidth can minimize noise but remain sufficiently broad to capture the relevant signal.

B.3 Test Procedures

B.3.1 Amplitude and Frequency Setup

1. Initiate a default configuration on LabOne, then open "Lock-in Tab (HF2-MF Option)".

2. In the "Signal Inputs" section, turn on AC Coupling and Differential Input settings for both Signal Input 1 and Signal Input 2.

3. In the "Oscillators" section, set oscillator 1 to 1MHz and adjust oscillator 2 to 54 kHz (or to the estimated natural frequency of the device).

4. In the "Demodulators" Section, enable "Data Transfer" for Demodulators 1,2,4,5, and set the data transfer rate to approximately 14k Sa/s (Note: Adjusting the data transfer rate does not impact real-time modulation).

5. In the "Output Amplitudes", enable Demodulator 8 Amplitude and set it to 500mV (This value might be refined in a subsequent step).

6. Open the "Mod Tab" from the right side of the LabOne Software Interface.

7. For "MOD 1", enable the modulation by selecting the toggle. In "Reference Frequencies", set the carrier to oscillator 1 (1 MHz) and sideband 1 to oscillator 2 (54 kHz). Under "Input", set the signal to Signal Input 1 to demodulate the signal with the reference signal. In "Generation", set the carrier voltage to 500mV and enable it (This initial value will be adjusted later to maximize the SNR).

8. For "Mod 2", repeat the same setting for "MOD 1", except in the "Input" section, set signal to Signal input 2.

9. Return to the "Lock-in Tab", in the "Demodulators" section, the demodulator values will now be in a read-only format. The relationship between the TRG electrodes, as illustrated in Fig. 3.3, and demodulators are tabulated in Table B.1.

B.3.2 Optimize SNR of Signal Inputs

1. Open the "Scope" Tab at the top of the interface and keep the "Lock-In" Tab at the bottom of the window. In the "Signal Outputs" section, set the range for both Output 1 and Output 2 to 1V, then turn on Output 1 and Output 2.

2. On the "Lock-In" Tab, in the "Signal Inputs" Section, click on the auto-adjust feature for "Input 1" and "Input 2" to enhance the resolution of the signal inputs.

Demodulators	Descriptions	Axis/Purpose
1	Carrier Frequency	X-axis/Drive
2	Carrier + Sideband	X-axis/Drive
3	Carrier - Sideband	X-axis/Drive
4	Carrier Frequency	Y-axis/Sense
5	Carrier + Sideband	Y-axis/Sense
6	Carrier - Sideband	Y-axis/Sense
7	Demodulation for PLL 1	Carrier (not adjusting carrier)
8	Demodulation for PLL 2	AC Signal Feedback Control (PLL/AGC)

Table B.1: Overview of Demodulators and Operating Parameters of TRG

3. On the "Scope" Tab, under the "Control" section, select Signal Inputs 1 and 2 to visualize the sensor signal output of the drive and sense mode. The display should reveal a modulated signal similar to that depicted in Fig. B.5. The voltage level for the carrier and AC driving may be higher or lower than the initial setting, potentially causing signal saturation or noise (See Fig. B.7). It is advisable to start by turning on just the Signal Output 1 (AC driving Signal). The signal should appear similar to what is illustrated in Fig. B.6.

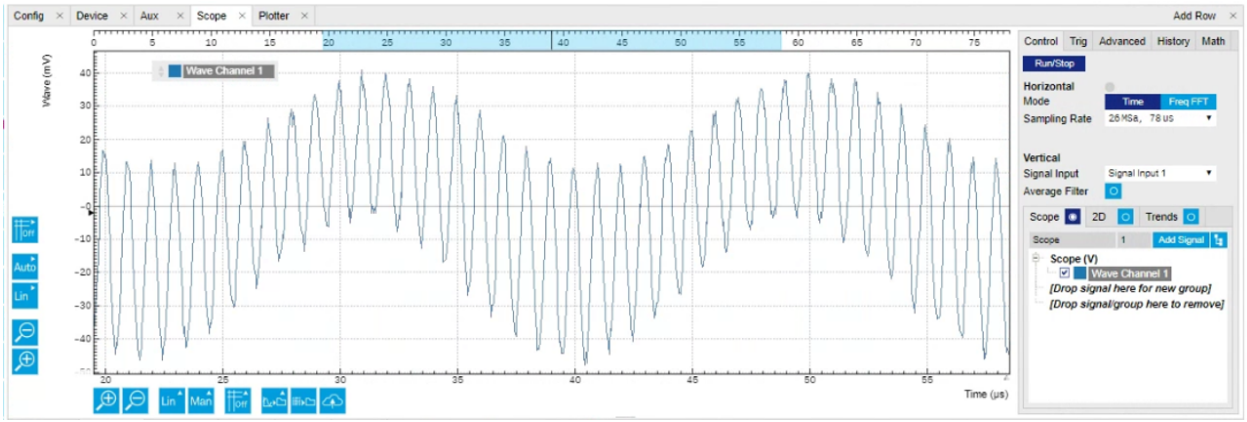

Figure B.5: AC driving signal with carrier signal, Signal Input 1 from the sensor to Zurich Instrument

B.3.3 Frequency Sweep to Obtain the Resonance Frequency of the Sensor

1. Once clear modulated signals are observed on both Signal Input 1 and Signal Input 2, the sensor is prepared for a frequency sweep. Open the 'Sweeper' tab located on the right side of the LabOne Interface.

2. Before performing a frequency sweep, go to "Settings" and click on "Advance" Mode. Adjust the "BW NEP (Hz)" to 20Hz or below to get a faster sweep. While it is not

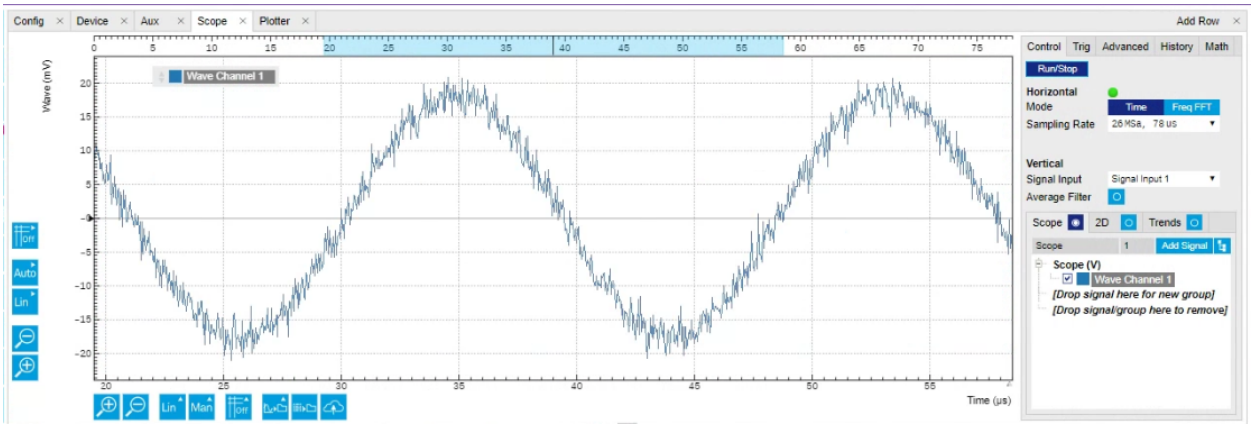

Figure B.6: AC driving signal detected from Signal Input 1

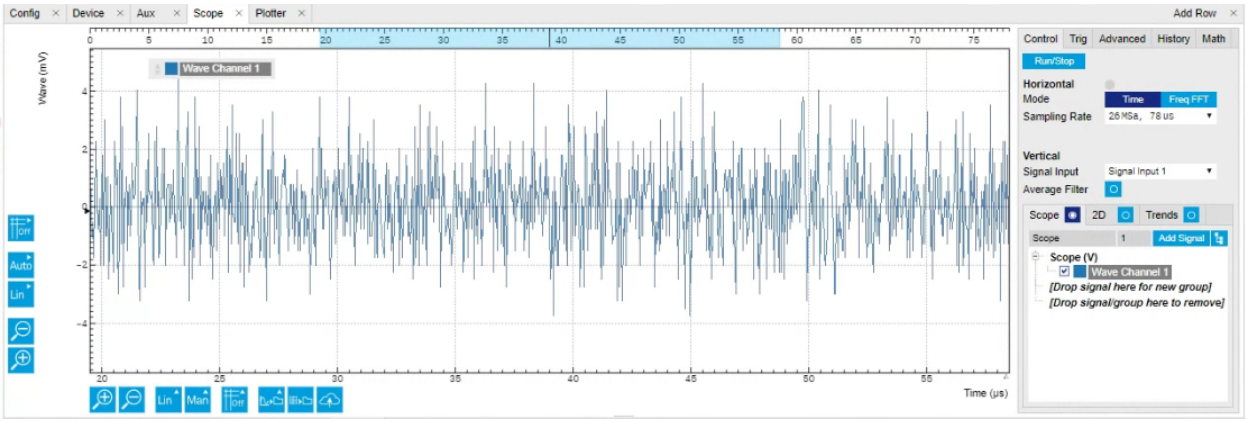

Figure B.7: Detected noise level is too high from Signal Input 1

mandatory, for a smoother sweep with finer resolution, set the minimum samples to 16 or 32 samples. The setting of the "Sweeper Tab" is shown in Fig. B.8.

3. Navigate back to the "Control Section" within the "Sweeper" Tab. Input "Start" and "Stop" Frequencies at 54.447 kHz and 54.480 kHz, respectively. If the resonant frequency of the sensor is unknown, consider starting with a broader frequency range for sweeping. Set "length (pts)" to "500" or smaller to expedite the sweep. This parameter can be adjusted to achieve either a finer or coarser sweep, with a tradeoff with the sweeping duration.

4. Select Sweep Parameter to "Osc 2 Frequency" to sweep the AC driving frequency and Choose "Demod R 2" and "Demod R 5" to add a signal to view the demodulated sidebands or the detected signals from the sensor. The setting for the Sweep Tab is shown in Fig. To view the sweep in the viewable range, click on the highlighted yellow box to "FS" and the highlighted red box to "Auto". See Fig. B.9 for the adjustments.

5. Before starting the sweep, ensure both Signal Output 1 and Signal Output 2 are on. Click "Single" on the upper right of the "Sweeper" Tab to sweep once. Monitor Demod 2 and Demod 5 for signs of a peak. If no obvious peaks or peaks are detected in the current sweep, try again with a different frequency sweep range until a frequency peak is observed for both Demod 2 and Demod 5. An example of the frequency peak is shown in Fig. B.10.

6. To extract the frequency and voltage value of peaks, select the "Math" Tab next to "History", and select "Peak" and "Position 1" to annotate the peak on the sweeper plot.

7. Document the voltage level and the frequency at which peaks occur for Demod 2 and Demod 5 Signals. These values will be used later for PLL and AGC.

8. Repeat the steps mentioned above, starting by disconnecting the BNC cable from Forcer X on the front-end electronics and then connecting it to Forcer Y to detect the peaks along the sense axis.

B.3.4 Phase-Locked Loop (PLL) Settings

1. Open the "Plotter" tab and position it on the top panel, and leave the "Lock-In" Tab at the bottom panel of the LabOne Interface.

2. In the "Plotter" tab, adjust the time length from "10 s" to "1 min" in the upper right corner. In the "Vertical" Section, click on "Enabled Demods R" to enable the settings for Demodulated signals. In the "Plotter" section, choose "Demod R 2" to display the demodulated signals of the sensor output. Adjust the vertical scale to "dB" and the horizontal scale to "Linear" on the plot.

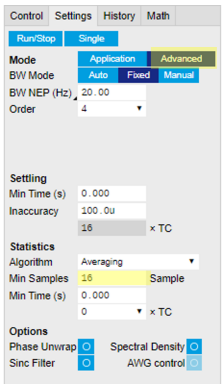

Figure B.8: LabOne Sweeper Settings

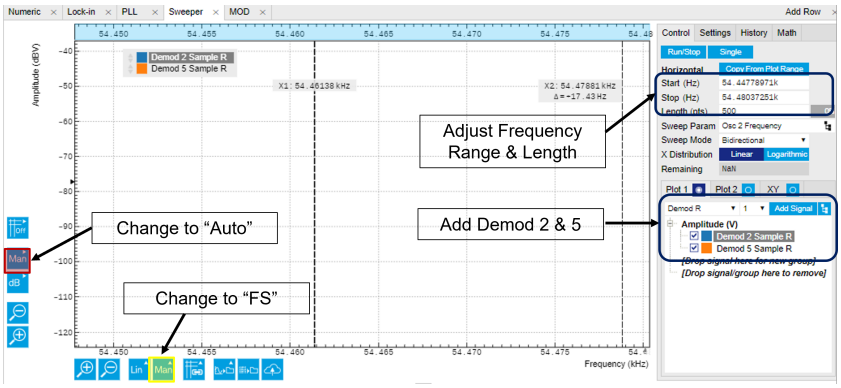

Figure B.9: LabOne Sweeper Tab Control Section

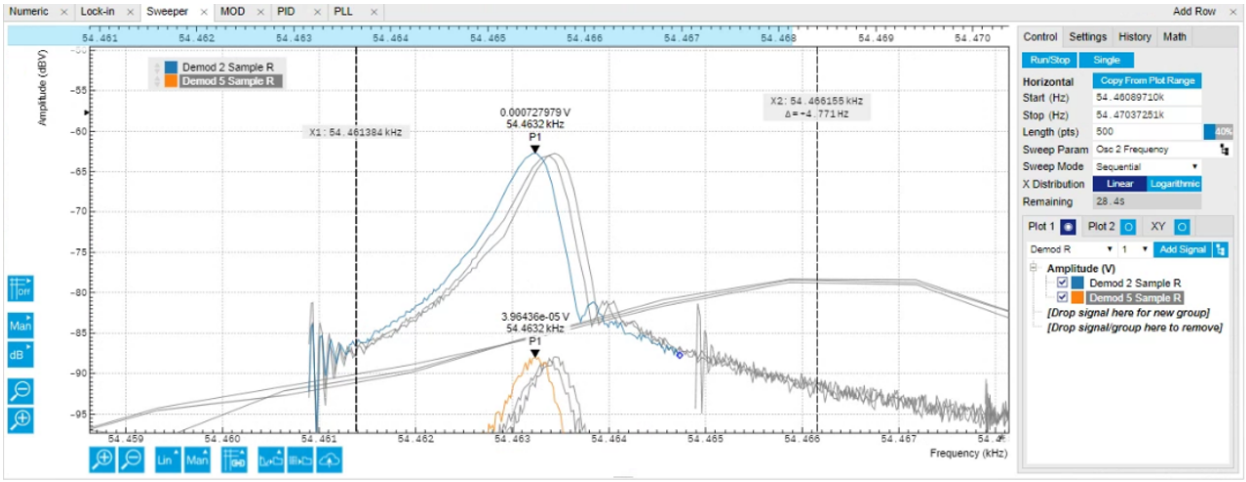

Figure B.10: LabOne Observed Frequency Peaks on Demod 2 and Demod 5

3. Copy the previously observed frequency peak and paste it into oscillator 2 on the "Lock-In" Tab. The amplitude of the "Demod 2" may change on the plotter and output a horizontal line.

4. Disable "Signal Output 1" to turn off the AC driving signal to the sensor. The demodulated signal will start to decay, reaching a lower level. Pause the plot in the "Plotter" tab by clicking on "Run/Stop" in the upper right-hand corner.

5. Measure the time difference on the plot when it decays from -8.68dBV and record the decay time to compute the quality factor using $Q = \pi \cdot \text{freq} \cdot \text{decay time}$. An estimated quality factor can be estimated, and this value will be used in the PLL advisor later.

6. Open the "PLL Tab" from the software interface on the right side. Select "PLL 2" instead of "PLL 1" to adjust the frequency values for demodulator 8. In the "PLL settings" section, change the "Input" to Aux in 1. Input the "center frequency" to the measured peak frequency from the sweeper tab.

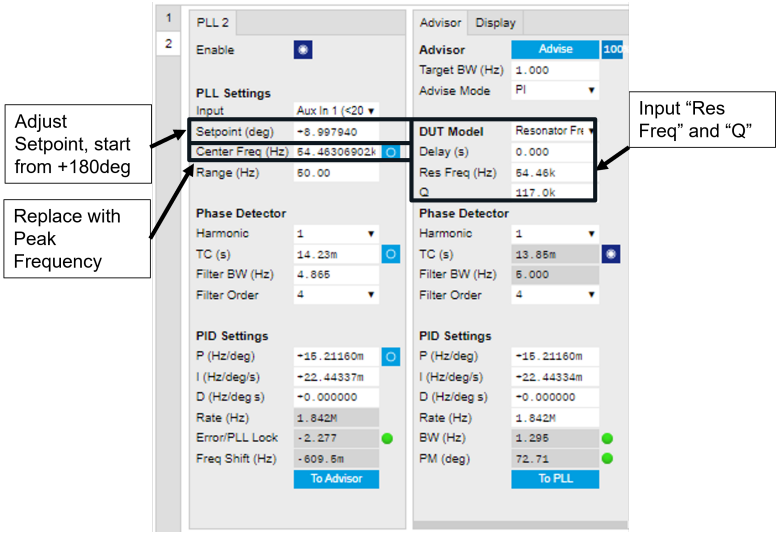

Figure B.11: LabOne PLL settings

7. In the "Advisor" section, choose "Resonator Frequency" for "DUT Model". Input the measured "Res Freq" and "Q" values. Click "Advise" to compute the estimated PI parameters. Adjust the "Target BW" value to 1 or lower. Ensure two green light indicators are on before pressing "To PLL" to transfer the estimated PI parameters to the PLL settings. The PLL settings should be similar to Fig. B.11.

8. Open the "Aux" Tab on the right side of the LabOne Interface. Select "Demod 1" for Aux 1 and use auto-zero for the input voltage amplitude until the Aux Voltage output is zero. Repeat this step if the PLL is not locked in the next step.

9. Return to the "PLL" tab and enable PLL 2 settings. Adjust the "Setpoint(deg)" from +180 degrees downwards by 10 degrees until the output amplitude of the demodulated signal is close to the previously recorded amplitude from the sweeper tab. The

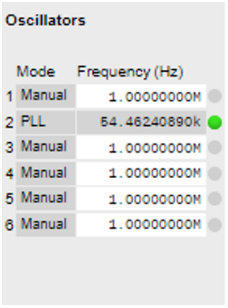

Figure B.12: PLL is locked and adjusting the frequency of the AC driving signal (Signal Output 1)

error/PLL lock should stay within 20 to lock the PLL with a green light on oscillator 2 in the "Lock-in" tab, as depicted in Fig. B.12.

For the TRG device referenced in this example, the demodulated signal increased from 0.1mV after the PLL was enabled, as demonstrated in Fig. B.13. After the PLL is locked with the green light indicator on, the response is stabilized at a constant amplitude close to the recorded amplitude in the sweeper tab, as shown in Fig. B.14.

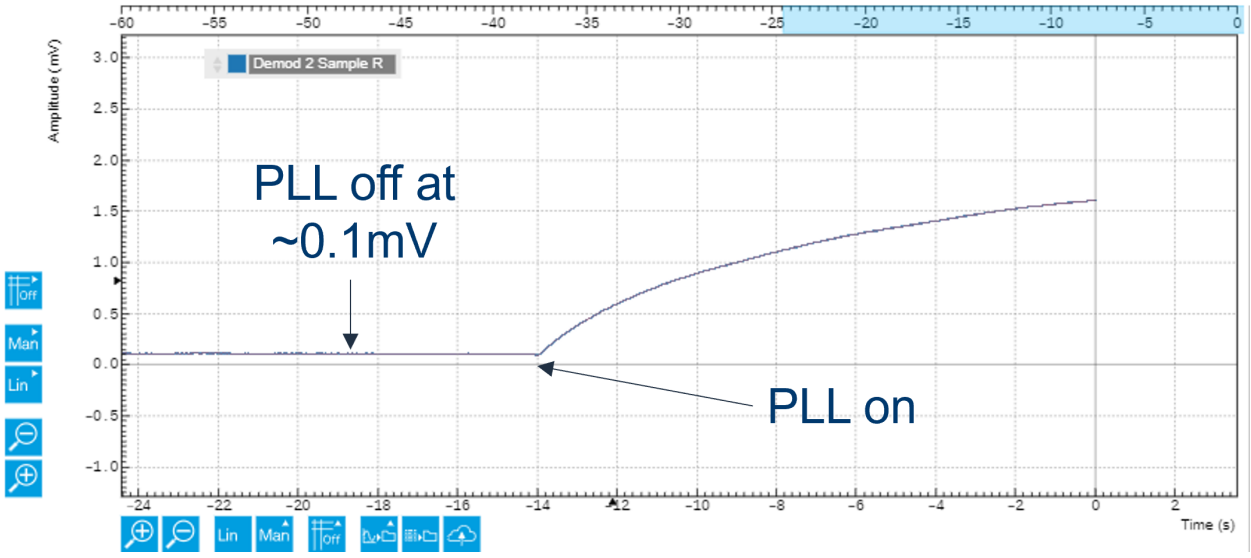

Figure B.13: Demodulated Signal response after PLL is enabled

B.3.5 Automatic Gain Control (AGC) Settings

1. Confirm that the PLL is locked with a green light displaying next to oscillator 2, as shown in Figure. XX. Note that Signal Output 1 amplitude is at 500mV, as illustrated in Fig. B.15. Open the "PID" Tab on the left side of the LabOne User Interface.

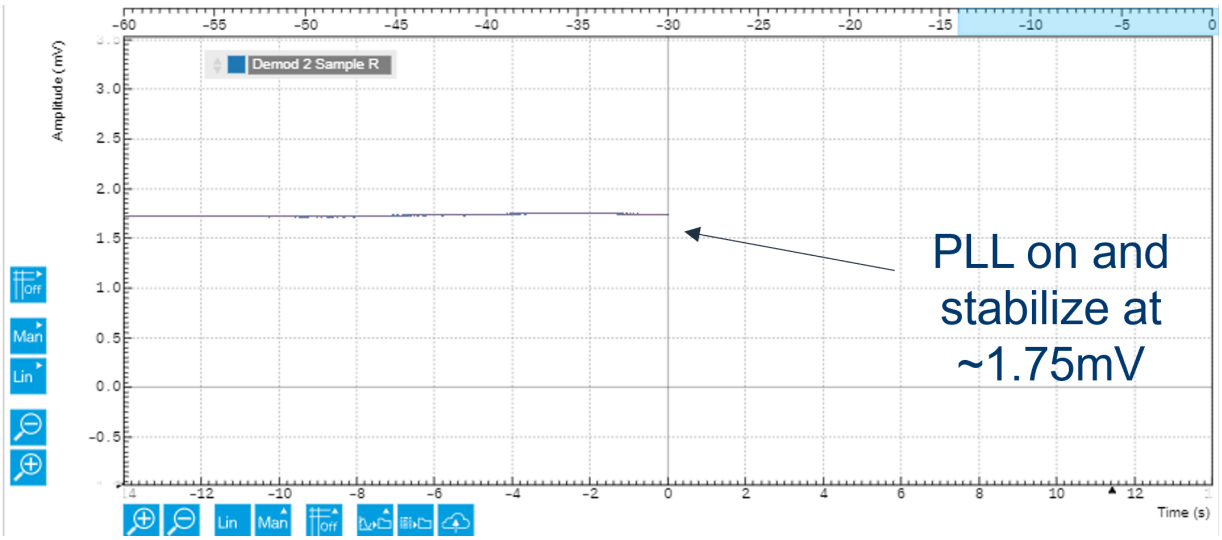

Figure B.14: Demodulated Signal is stabilized after the PLL is locked with green light indicator on

2. The PID tab contains 4 built-in PID settings for adjustment. Select any PID tab to modify the setting. Under the "Input" section, set the input signal to "Demod R 2" and adjust the "Setpoint (V)" to 428u. This value can be varied by the user to control the output amplitude from the sensor.

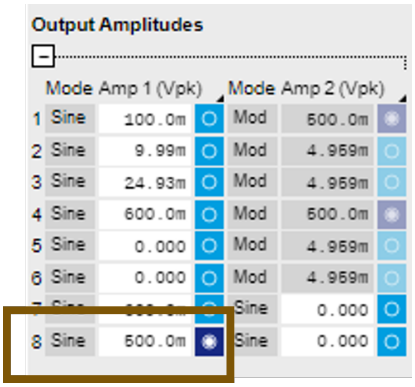

Figure B.15: LabOne AC signal output at 500mV initially

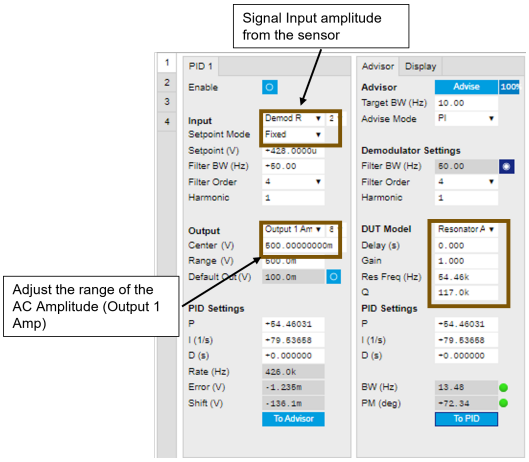

Figure B.16: LabOne PID Settings

3. In the "Output" section, select "Output 1 Amp 8" to allow the PID setting to adjust the AC Signal (Signal Output 1) driving the sensor. The "Center" voltage and "Range" can be set by the user to limit the minimum and maximum value of the AC signal. Set the "Center" to 500mV and the "Range" to 500mV, so the minimum output amplitude is 250mV, and the maximum output amplitude is 750mV.

4. Navigate to "PID Advisor" on the right side of the PID settings. Under "DUT Model",

select “Resonator Amplitude”, and input the “Res Freq” and “Q” obtained from the frequency sweep plots.

5. Click on “Advice” to obtain the estimated PID values for the PID settings. Adjust the “Target BW (Hz)” if necessary until a green light appears at the bottom for BW (Hz). Once two green lights are shown for the BW (Hz) and PM (deg) values at the bottom, click on “To PID” to transfer the calculated PI parameters to the PID Setting. Fig. B.16 displays the PID setting for adjusting the amplitude.

6. Enable the current PID settings. Under the “Lock-In” Tab, the output amplitude for demodulator 8 is automatically changed from “Sine” to “PID”, as shown in Fig. B.17. The output amplitude value will be gradually adjusted until the sensor output amplitude (demodulated signal amplitude) reaches the desired setpoint value (428uV) input in the PID setting. Fig. B.18 shows the “Demod 2 R” output amplitude starting to adjust after the AGC is enabled. The time response of the sensor output after it reaches a constant amplitude is indicated in Fig. B.19.

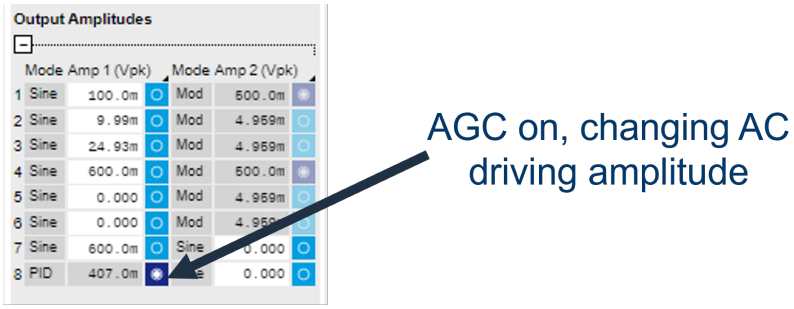

Figure B.17: LabOne AC Signal Output changed from “Sine” to “PID” defined values

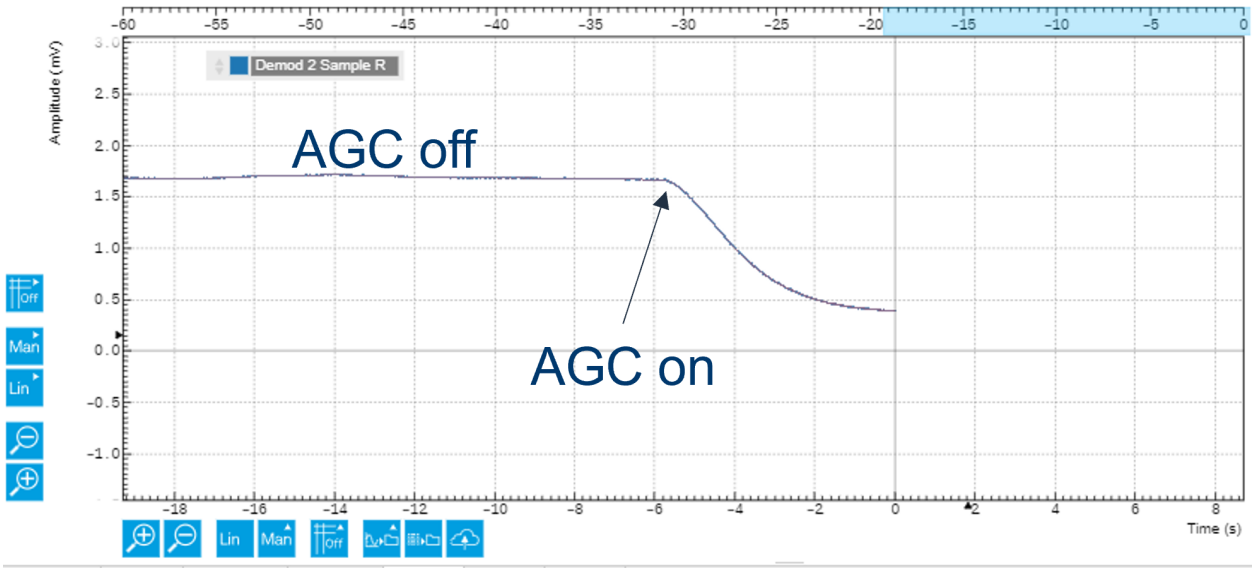

Figure B.18: Demodulated Signal Amplitude changes after Automatic Gain Control is enabled

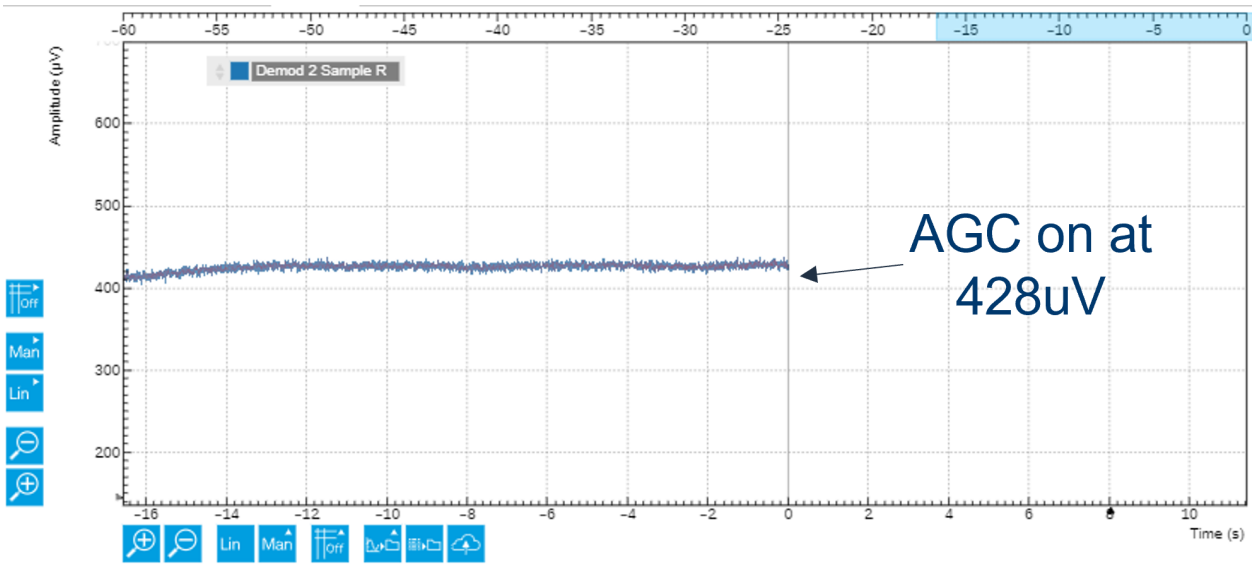

Figure B.19: Demodulated Signal Amplitude is maintained at 428uV